

TIME-DEPENDENT, COMPOSITIONALLY DRIVEN CONVECTION IN THE OCEANS OF ACCRETING NEUTRON STARS

ZACH MEDIN

Los Alamos National Laboratory, Los Alamos, NM 87545, USA

AND

ANDREW CUMMING

Department of Physics, McGill University, 3600 rue University, Montreal, QC, H3A2T8, Canada

Draft version July 27, 2018

ABSTRACT

We discuss the effect of chemical separation as matter freezes at the base of the ocean of an accreting neutron star, and the subsequent enrichment of the ocean in light elements and inward transport of heat through convective mixing. We extend the steady-state results of Medin & Cumming (2011) to transiently accreting neutron stars, by considering the time-dependent cases of heating during accretion outbursts and cooling during quiescence. Convective mixing is extremely efficient, flattening the composition profile in about one convective turnover time (weeks to months at the base of the ocean). During accretion outbursts, inward heat transport has only a small effect on the temperature profile in the outer layers until the ocean is strongly enriched in light elements, a process that takes hundreds of years to complete. During quiescence, however, inward heat transport rapidly cools the outer layers of the ocean while keeping the inner layers hot. We find that this leads to a sharp drop in surface emission at around a week followed by a gradual recovery as cooling becomes dominated by the crust. Such a dip should be observable in the light curves of these neutron star transients, if enough data is taken at a few days to a month after the end of accretion. If such a dip is definitively observed, it will provide strong constraints on the chemical composition of the ocean and outer crust.

Subject headings: dense matter — stars: neutron — X-rays: binaries — X-rays: individual

1. INTRODUCTION

The outermost $\simeq 30$ m of an accreting neutron star is expected to form a fluid ocean that overlies the kilometer-thick solid crust of the star (Bildsten & Cutler 1995). This ocean is of interest as the site of long duration thermonuclear flashes such as superbursts (Cumming & Bildsten 2001; Strohmayer & Brown 2002; Kuulkers et al. 2004) and intermediate duration bursts (in 't Zand et al. 2005; Cumming et al. 2006), non-radial oscillations (Bildsten & Cutler 1995; Piro & Bildsten 2005) and because the matter in the ocean eventually solidifies as it is compressed to higher densities by ongoing accretion, and so determines the thermal, mechanical and compositional properties of the neutron star crust (Haensel & Zdunik 1990; Brown & Bildsten 1998; Schatz et al. 1999). The thermal properties of the ocean determine the initial cooling of an accreting neutron star following the onset of quiescence (Brown & Cumming 2009, hereafter BC09) as observed for 6 sources (Wijnands et al. 2001, 2002, 2003, 2004; Cackett et al. 2006; Homan et al. 2007; Cackett et al. 2008; Fridriksson et al. 2011; Degenaar & Wijnands 2011; Degenaar et al. 2011, 2013b; Cackett et al. 2013).

The composition of the ocean is expected to consist of mostly heavy elements, formed by rapid proton capture (the rp-process) during nuclear burning of the accreted hydrogen and helium at low densities and subsequent electron captures at higher densities, although some carbon may also be present (Schatz et al. 2001;

Gupta et al. 2007). At the ocean-crust boundary, as the matter transitions from liquid to solid it also undergoes chemical separation. Numerical simulations of phase transitions in neutron stars (Horowitz, Berry, & Brown 2007) have shown that as the ocean mixture solidifies, the lighter elements (charge numbers $Z \lesssim 20$) are preferentially left behind in the liquid whereas the heavier elements are preferentially incorporated into the solid. In Medin & Cumming (2011) (hereafter Paper I), we showed that the retention of light elements in the liquid acts as a source of buoyancy that drives a continual mixing of the ocean, enriching it substantially in light elements and leading to a relatively uniform composition with depth. Heat is also transported inward to the ocean-crust boundary by this convective mixing. In Medin & Cumming (2014) (hereafter Paper II) we showed that during quiescence the inward heat transport is particularly strong, leading to rapid cooling of the outer ocean and a significant drop in the light curve compared with standard cooling models (e.g., BC09).

One motivation for studying the problem of “compositionally driven” convection in the neutron star ocean comes from superbursts, which are thought to involve thermally unstable carbon burning in the deep ocean of the neutron star (Cumming & Bildsten 2001; Strohmayer & Brown 2002). The energy release in these very long duration thermonuclear flashes, inferred from fitting their light curves (Cumming et al. 2006), corresponds to carbon fractions of $\approx 20\%$. This has been challenging to produce in models of the nuclear burning of the accreted hydrogen and helium. If the hydrogen and helium burn unstably, the amount of carbon produced is

$\lesssim 1\%$ (Woosley et al. 2004), and whereas stable burning can produce large carbon fractions (Schatz et al. 2003; Stevens et al. 2014), time-dependent models do not show stable burning at the $\approx 10\%$ Eddington accretion rates of superburst sources (although observationally, superburst sources show evidence that much of the accreted material may not burn in Type I bursts; in 't Zand et al. 2003). Perhaps even more problematic than making enough carbon is that carbon ignition models for superbursts require large ocean temperatures $\approx 6 \times 10^8$ K at the ignition depth, which are difficult to achieve in standard models of crust heating (e.g., Brown 2004; Cumming et al. 2006; Keek et al. 2008).

Observations of quiescent transiently accreting neutron stars also provide strong motivation for studying ocean convection. BC09 inferred a large inward heat flux in the outer crust of the sources MXB 1659–29 and KS 1731–260 by fitting their light curves in quiescence. Other anomalous behavior from transiently accreting neutron stars includes a rebrightening during a cooling episode in XTE J1701–462 (Fridriksson et al. 2011), and very rapid cooling a few days after accretion shut off in XTE J1709–267 (Degenaar et al. 2013b). Though both the rebrightening and the rapid cooling can be explained by a spurt of accretion during quiescence, as we show here these features may naturally arise from the cooling ocean when chemical separation occurs.

In this paper we generalize and expand on the results of Papers I and II: We place the steady-state calculations of Paper I in a larger context by adding the relevant physics into a full envelope-ocean-crust model (cf. Brown 2004; BC09; Paper II) and by considering the evolution toward that steady state; and we examine the quiescence calculations of Paper II in greater detail and provide cooling curve fits for several additional sources. We begin in Section 2 by reviewing the picture of steady-state, compositionally driven convection as presented in Paper I, and discuss how the picture changes when time dependence is considered. In Section 3 we describe our calculation of the time-dependent temperature and composition structure of the ocean and crust. In Sections 4 and 5 we present results from our calculation during accretion and during cooling after accretion turns off, respectively; in Section 5.1 we additionally provide an analytic approximation to our cooling model. In Section 6 we compare the cooling light curves we generate to observations of transiently accreting neutron stars during quiescence. Finally, in Section 7 we discuss the implications of our results.

2. COMPOSITIONALLY DRIVEN CONVECTION IN THE OCEAN

2.1. Phase diagrams and chemical separation

As in Paper I, to understand the effect of compositionally driven convection on the ocean we first consider the phase diagram for the ocean mixture. Though the ocean in an accreting neutron star is likely made up of a wide variety of elements (Schatz et al. 2001; Gupta et al. 2007), for computational tractability we only consider a two-component mixture of oxygen and selenium in this paper. Our O-Se mixture is modeled after the 17-component, rp-process ash mixture considered by Horowitz et al. (2007) (see also Gupta et al. 2007); in that latter mixture selenium is the most abundant ele-

ment and oxygen is the most abundant low- Z element. While the relative abundances and mass numbers of each element change with depth due to electron captures, we ignore any such effects and use ^{16}O – ^{79}Se throughout the ocean. It is unclear whether including two components is enough to accurately model the effects of chemical and phase separation in the ocean, and if so, what the charge values of those two components should be. Calculations of multicomponent phase diagrams using both extrapolation (cf. Medin & Cumming 2010) and molecular dynamics techniques (e.g., Hughto et al. 2012) are in progress to address these issues. Note that the equations in the body of the paper are specific to two-component mixtures, but that unless otherwise specified the equations in the Appendix are applicable generally to multicomponent mixtures.

The Coulomb coupling parameter is an important quantity for determining the phase diagram of two-component mixtures. The Coulomb coupling parameter for ion species i is

$$\Gamma_i = \frac{Z_i^{5/3} e^2}{k_B T} \left(\frac{4\pi\rho Y_e}{3m_p} \right)^{1/3}, \quad (1)$$

while that for the mixture is

$$\begin{aligned} \Gamma &= \frac{\langle Z^{5/3} \rangle e^2}{k_B T} \left(\frac{4\pi\rho Y_e}{3m_p} \right)^{1/3} \\ &= 204 \rho_9^{1/3} \left(\frac{T_8}{3} \right)^{-1} \left(\frac{\langle Z^{5/3} \rangle}{357} \right) \left(\frac{Y_e}{0.43} \right)^{1/3}. \end{aligned} \quad (2)$$

Here Z and A are the ion charge and mass number, $Y_e = \langle Z \rangle / \langle A \rangle$ is the electron fraction, $\rho_9 = \rho / (10^9 \text{ g cm}^{-3})$ the density, and $T_8 = T / (10^8 \text{ K})$ the temperature; $\langle Q \rangle$ signifies the number average of quantity Q for the mixture, such that $\langle Q \rangle = x_1 Q_1 + x_2 Q_2$, where x_i is the number fraction of species i .

Figure 1 shows two phase diagrams for a two-component mixture with charge ratio $Z_2/Z_1 = 34/8 = 4.25$, appropriate for, e.g., an oxygen-selenium mixture (charge ratio 4.25). The top panel shows the detailed phase diagram calculated in Medin & Cumming (2010); the bottom panel shows the approximate phase diagram used in the calculations in this paper. In each panel, the x-axis shows x_2 , the number fraction of the heavier ion species, and the left y-axis shows Γ_1^{-1} , the inverse of the Coulomb coupling parameter for the lighter species. For reference, the right y-axis shows Γ_2^{-1} , the inverse of the coupling parameter for the heavier species. In addition, “L” denotes the stable liquid region, “S1” and “S2” denote stable solid regions, and the shaded region represents the unstable region of the phase diagram. A parcel with composition and temperature (or equivalently, x_2 and Γ_1) that lies inside the unstable region will undergo phase separation, separating into two phases with compositions on either side of the unstable region.¹ In this way, chemical separation occurs.

For a single species of ion, solidification occurs when $\Gamma > \Gamma_{\text{crit}} \approx 175$ (e.g., Potekhin & Chabrier 2000). For

¹ In the special case that Γ_1 is at its eutectic value, the parcel separates into three phases; for the example of Fig. 1, when $\Gamma_{\text{crit}}/\Gamma_1 = 3.6$, the parcel separates into L, S1, and S2. See Paper I.

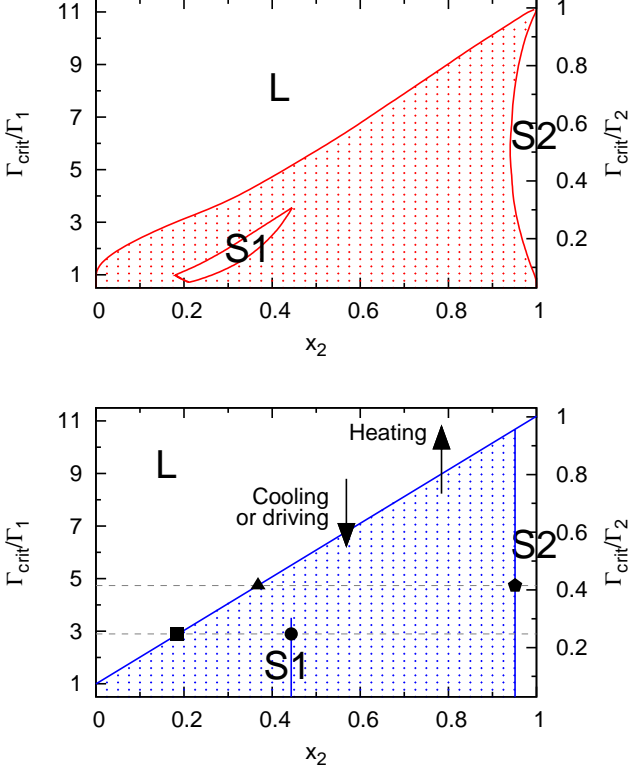


FIG. 1.— The phase diagram for crystallization of a two-component mixture with charge ratio $Z_2/Z_1 = 34/8$ (top panel), and its approximation as used in our simulation (bottom panel). The Coulomb coupling constants Γ_1 and Γ_2 are given in terms of $\Gamma_{\text{crit}} \approx 175$, the value at which a single-species plasma crystallizes. The stable liquid region of each phase diagram is labeled “L”, the stable solid regions are labeled “S1” and “S2”, and the unstable region is filled with plus symbols. A particle in the ocean/crust moves down the phase diagram during cooling or accretion driving, and up during rapid heating. In the bottom panel, the liquid composition marked by a filled triangle is in equilibrium with the solid composition marked by a filled pentagon; the liquid composition marked by a filled square is in equilibrium with the solid composition marked by a filled circle.

a multicomponent mixture a liquid becomes unstable to phase separation at a Γ value that varies with composition, known as the liquidus curve (in Fig. 1, the upper boundary of the unstable region). For the $Z_2/Z_1 = 4.25$ charge mixture shown in Fig. 1 the liquidus curve is almost linear in Γ_1^{-1} vs. x_2 , with $\Gamma \simeq \Gamma_{\text{crit}}$; we have therefore chosen $\Gamma = \Gamma_{\text{crit}}$ as the liquidus curve for our approximate phase diagram. Using Eq. (2) and the equation of state of relativistic, degenerate electrons (applicable for $\rho \gtrsim 10^7 \text{ g cm}^{-3}$)

$$y = \frac{P}{g} = \frac{(3\pi^2)^{1/3} \hbar c}{4g} \left(\frac{\rho Y_e}{m_p} \right)^{4/3}, \quad (3)$$

where y is the column depth, P is the pressure, and g is the surface gravity, we have that the liquidus in our phase diagram corresponds to the column depth

$$y_L = \left[\frac{3}{16} \left(\frac{9}{4\pi^2} \right)^{1/3} \frac{\hbar c}{g} \left(\frac{\Gamma_{\text{crit}} k_B T}{\langle Z^{5/3} \rangle e^2} \right)^4 \right]_L, \quad (4)$$

where T and $\langle Z^{5/3} \rangle$ are evaluated at the liquidus. Al-

though a multicomponent liquid becomes unstable to phase separation at the liquidus, in general it does not completely solidify until a much larger value of Γ . However, we found in Paper I that in the neutron star ocean any liquid-solid mixture formed during phase separation will differentiate spatially due to sedimentation of the solid particles at a rate much faster than any of the other mixing processes (including accretion driving).² This means that all of the liquid in the ocean-crust region will lie above all of the solid there, such that the liquid effectively solidifies at the liquidus; the liquidus depth is also the depth of the ocean-crust boundary y_b . In other words, from Eq. (4)

$$y_b \equiv y_L \quad (5)$$

$$= 5.57 \times 10^{12} \left(\frac{T_{b,8}}{3} \right)^4 \left(\frac{\langle Z_b^{5/3} \rangle}{357} \right)^{-4} \left(\frac{g_{14}}{2.45} \right)^{-1} \text{ g cm}^{-2}, \quad (6)$$

where T_b and Z_b are the temperature and ion charge at the base of the ocean.

2.2. Regimes of chemical separation

The fate of ocean-crust particles as they cross into the unstable region of the phase diagram and undergo phase/chemical separation is determined by the composition of the parcels before crossing and the direction they are moving on the diagram. The initial composition of the parcels depends on the accretion history of the neutron star. The direction each parcel moves on the phase diagram depends on whether accretion is ongoing or not; and if accretion is ongoing, whether the rate at which the ocean-crust boundary moves inward is greater than the rate at which particles are driven inward, i.e., whether $\dot{y}_b > \dot{m}$, where \dot{y}_b is the rate of change in y_b and \dot{m} is the local accretion rate per unit area. There are three regimes to consider: steady-state accretion, cooling after accretion shuts off, and rapid heating shortly after accretion turns on.

1) When the neutron star is accreting and the ocean-crust system is near or at its steady-state configuration, $\dot{y}_b < \dot{m}$. In this regime accreted material is driven to higher pressure, such that material at the base of the ocean moves across the ocean-crust boundary and freezes (as shown by the arrow marked “driving” in Fig. 1). According to the simplified phase diagram in Fig. 1, if the ocean base has a composition $x_2 > 0.95$ or $x_2 = 0$, there will be no chemical separation upon freezing. If $0.95 > x_2 > 0.25$, some material will remain liquid and some will form a solid of composition S2. If $0.25 > x_2 > 0$, some material will remain liquid and some will form a solid of composition S1.

2) When accretion turns off and the neutron star is cooling, $\dot{y}_b < 0$ and $\dot{m} = 0$. In this regime the temperature drops in the ocean, such that the ocean-crust boundary moves outward and the base of the ocean freezes (“cooling” in Fig. 1). In this case the behavior of chemical separation with x_2 will be the same as that described above.

² This requires the solid particles to be denser than the liquid, which for the phase diagram shown in Fig. 1 is true at all compositions except x_1 very close to unity.

3) When accretion turns on again and the system moves toward its steady-state configuration, the heating is initially very strong. In this regime the crust melts faster than new material can be driven across the ocean-crust boundary, such that $\dot{y}_b > \dot{m}$ (and material follows the “heating” arrow in Fig. 1). According to our simplified phase diagram, if the crust has a composition $x_2 = 0$, $x_2 > 0.95$, or S2, there is no chemical separation of the solid upon melting. If the crust is of composition S1, there will be chemical and phase separation into a light liquid and an S2 solid. However, assuming diffusion between solid-solid phases is slow (cf. Hughto et al. 2011), as heating continues the liquid and the solid will travel together up the phase diagram until the solid melts and recombines with the liquid; since the distance over which this occurs is relatively short compared to the size of the ocean, we assume for simplicity that in our calculations a solid of composition S1 will just melt to form a liquid of composition S1 ($x_2 = 0.44$). Therefore, in our calculations there is no chemical or phase separation when $\dot{y}_b > \dot{m}$, regardless of crust composition.

2.3. Compositional buoyancy and convection

What happens to the liquid left behind after phase separation and sedimentation of the solid depends on its composition. During rapid heating (regime 3 of the previous subsection) the liquid remains in place at the base of the ocean, since it is heavier than or at the same composition as the liquid above it. During steady-state accretion or cooling (regimes 1 and 2), however, after the solid particles form and sediment out the liquid left behind is lighter than the liquid immediately above it and so will have a tendency to buoyantly rise. This is counteracted by the thermal profile, which is stably stratified in the absence of a composition gradient such that a rising fluid element will be colder than its surroundings and will tend to sink back down.

A measure of the buoyancy is the convective (Schwarzschild) discriminant \mathcal{A} , which is related to the Brunt-Väisälä frequency $N^2 = -g\mathcal{A}$ (Cox 1980). In Appendix A we derive the equations for convective stability; for a two-component mixture we can write [Eq. (A7); see also Kippenhahn & Weigert 1994]

$$\mathcal{A}H_P\chi_\rho = \chi_T(\nabla - \nabla_{\text{ad}}) + \chi_1\nabla_{X_1}. \quad (7)$$

Here,

$$\chi_1 = \chi_{X_1} - \chi_{X_2}\frac{X_1}{X_2} + \chi_{Y_e}\frac{(Y_1 - Y_2)X_1}{Y_e}, \quad (8)$$

$X_i = x_i A_i / \langle A \rangle$ is the mass fraction of species i , $Y_i = Z_i / A_i$ is the electron fraction of species i , $H_P = -dr/d\ln y = y/\rho$ is the scale height, and $\nabla = -H_P(d\ln T/dr)$ and $\nabla_{X_i} = -H_P(d\ln X_i/dr)$ are the temperature and composition gradients. The adiabatic temperature gradient is taken at constant (specific) entropy s and composition $\{X_i\}$: $\nabla_{\text{ad}} = -H_P(d\ln T/dr)_{s, X_1, X_2, Y_e}$. For a quantity Q , $\chi_Q = (\partial \ln Q / \partial \ln Q)$ with the other independent thermodynamic variables held constant. Although neither X_2 nor Y_e are independent variables, being subject to the constraints $X_2 = 1 - X_1$ and $Y_e = Y_1 X_1 + Y_2 X_2$, here we treat them as such in order to show explicitly the ion and electron contributions to various expressions in this

paper (e.g., the specific heat given below). The ion and electron contributions are then combined in Eqs. (8) and (16). Note that χ_1 , χ_T , and χ_ρ are all positive quantities. If $\mathcal{A} < 0$ or $N^2 > 0$ the ocean is stable to convection. For example, if the composition is uniform so that $\nabla_{X_1} = 0$, stability to convection requires the familiar condition $\nabla < \nabla_{\text{ad}}$. The maximum value of $\chi_1 \nabla_{X_1}$ such that the ocean is stable to convection is therefore $\chi_T(\nabla_{\text{ad}} - \nabla)$.

As steady-state accretion or cooling continues, light elements are continually deposited at the base of the ocean and must be transported upwards by convection. For efficient convection \mathcal{A} adjusts to be close to but slightly greater than zero. In Paper I we found that convection is extremely efficient throughout the ocean during steady-state accretion; in Appendix B of this paper we demonstrate that convection in the ocean is extremely efficient even during time-dependent heating or cooling, and even when effects due to rapid rotation ($\sim 10^2 \text{ s}^{-1}$) and moderate magnetic fields ($\sim 10^{10} \text{ G}$) are considered. We therefore assume in the main body of the paper that

$$\chi_1 \nabla_{X_1} = \chi_T(\nabla_{\text{ad}} - \nabla) \quad (9)$$

where convection is active (i.e., across the ocean convection zone).

2.4. Convection equations

Here we assume Newtonian physics, plane-parallel geometry, mixing length theory, and efficient convection [Eq. (9)]. In mixing length theory the value of the mixing length is highly uncertain; but note below that under the efficient convection assumption this parameter does not appear in our equations. The continuity equation for the flow of species i is given by

$$\frac{\partial X_i}{\partial t} + \dot{m} \frac{\partial X_i}{\partial y} = \frac{\partial F_{r, X_i}}{\partial y} + \epsilon_{X_i}, \quad (10)$$

where $\mathbf{F}_{X_i} = F_{r, X_i} \hat{\mathbf{r}}$ is the composition flux for species i and ϵ_{X_i} is the sum of all composition sources. The entropy balance equation is given by (e.g., Brown & Bildsten 1998)

$$T \frac{\partial s}{\partial t} + T \dot{m} \frac{\partial s}{\partial y} = \frac{\partial F_r}{\partial y} + \epsilon, \quad (11)$$

where

$$\mathbf{F} = F_r \hat{\mathbf{r}} = \mathbf{F}_{\text{cd}} + \mathbf{F}_{\text{conv}} \quad (12)$$

is the total flux,

$$\mathbf{F}_{\text{cd}} = F_{r, \text{cd}} \hat{\mathbf{r}} = \frac{KT}{H_P} \nabla \hat{\mathbf{r}} \quad (13)$$

is the conductive heat flux, $\mathbf{F}_{\text{conv}} = F_{r, \text{conv}} \hat{\mathbf{r}}$ is the convective heat flux, K is the thermal conductivity, and ϵ is the sum of all heat sources. The terms on the left-hand side of Eq. (11) can be written [Eqs. (A14) and (A13)]

$$T \frac{\partial s}{\partial t} = c_P \frac{\partial T}{\partial t} - \frac{b_1 T}{X_1} \frac{\partial X_1}{\partial t} \quad (14)$$

and

$$T \dot{m} \frac{\partial s}{\partial y} = \frac{c_P T \dot{m}}{y} \left(\nabla - \nabla_{\text{ad}} - \frac{b_1}{c_P} \nabla_{X_1} \right), \quad (15)$$

where $c_P = T(\partial s/\partial T)_{P,X_i,Y_e}$ is the specific heat capacity,

$$b_1 = b_{P,1} - b_{P,2} \frac{X_1}{X_2} + b_{P,e} \frac{(Y_1 - Y_2)X_1}{Y_e}, \quad (16)$$

$b_{P,i} = X_i(\partial s/\partial X_i)_{T,P,X_{j \neq i},Y_e}$, and $b_{P,e} = Y_e(\partial s/\partial Y_e)_{T,P,X_1,X_2}$. With the assumption of efficient convection, the convective heat flux in the ocean becomes [Eq. (B8)]

$$F_{r,\text{conv}} = -\frac{c_P T \chi_1}{X_1 \chi_T} \left(1 + \frac{\chi_T b_1}{\chi_1 c_P}\right) F_{r,X_1}, \quad (17)$$

the entropy balance equation in the ocean becomes [Eq. (B10)]

$$\begin{aligned} & c_P \frac{\partial T}{\partial t} + \frac{c_P T \chi_1}{X_1 \chi_T} \frac{\partial X_1}{\partial t} \\ &= \frac{\partial F_{r,\text{cd}}}{\partial y} - F_{r,X_1} \frac{\partial}{\partial y} \left[\frac{c_P T \chi_1}{X_1 \chi_T} \left(1 + \frac{\chi_T b_1}{\chi_1 c_P}\right) \right] + \epsilon, \end{aligned} \quad (18)$$

and the entropy advection term in the ocean becomes

$$T \dot{m} \frac{\partial s}{\partial y} = -\frac{c_P T \dot{m} \chi_1}{y \chi_T} \left(1 + \frac{\chi_T b_1}{\chi_1 c_P}\right) \nabla_{X_1}. \quad (19)$$

The steady-state versions of the above equations are similar to the convection equations from Paper I. Using Eq. (17) with the steady-state composition flux $F_{r,X_i} = \dot{m}(X_i - X_{i,0})$ [Paper I or Eq. (34)], we have that the steady-state convective flux is given by

$$F_{r,\text{conv}} = -\frac{c_P T \dot{m} \chi_1}{\chi_T} \left(1 + \frac{\chi_T b_1}{\chi_1 c_P}\right) \left(1 - \frac{X_{1,0}}{X_1}\right). \quad (20)$$

This equation differs from equation 43 of Paper I (which is in error) by the factor $1 + (\chi_T/\chi_1)(b_1/c_P)$, which is less than 1.2 in any part of the ocean; the extra factor does not qualitatively change the results of our earlier paper. In the deep ocean, because c_P , T , χ_1 , X_1 , and b_1 have only a weak dependence on y but $\chi_T \propto E_F \propto y^{-1/4}$, we also have that

$$F_{r,\text{conv}} \propto y^{1/4} \quad (21)$$

(cf. the result during cooling, $F_{r,\text{conv}} \propto y^{5/4}$; see Paper II) and

$$\frac{\partial F_{r,\text{conv}}}{\partial y} \simeq \frac{c_P T \dot{m} \chi_1}{4 y \chi_T} \left(1 - \frac{X_{1,0}}{X_1}\right). \quad (22)$$

Since $\nabla_{X_1} \ll 1$, we have from Eqs. (19) and (22) that $T \dot{m}(\partial s/\partial y) \ll \partial F_{r,\text{conv}}/\partial y$. Therefore, using Eq. (11) we have that

$$\frac{\partial F_r}{\partial y} \equiv \frac{\partial F_{r,\text{cd}}}{\partial y} + \frac{\partial F_{r,\text{conv}}}{\partial y} \simeq -\epsilon \quad (23)$$

in steady state, as we assumed in Paper I.

3. A MODEL OF THE ENVELOPE, CRUST, AND OCEAN IN THE TIME-DEPENDENT CASE

In our model we place the top of the envelope at $y = 10^{-4} \text{ g cm}^{-2}$ (i.e., at the surface) and the base of the crust at $y = 3 \times 10^{18} \text{ g cm}^{-2}$. The envelope structure is found as in Brown et al. 2002 (see also Potekhin et al. 1999). We assume an $\{X_H, X_{\text{He}}\} = \{0.7, 0.3\}$ composition throughout the envelope. The crust structure

and composition is found as in BC09, except that we leave the core temperature T_c as a free parameter rather than solving for it self-consistently, and use Newtonian physics with a surface gravity g constant across the envelope, ocean, and crust. General relativistic corrections are included only as an overall redshift of the time, $t_\infty = t(1 + z_{\text{surf}})$, and effective temperature, $T_{\text{eff},\infty} = T_{\text{eff}}/(1 + z_{\text{surf}})$, from the local value to that seen by an observer at infinity; here the neutron star mass and radius are $1.62 M_\odot$ and 11.2 km , giving a redshift factor of $1 + z_{\text{surf}} = 1.32$. Note that while g varies by about ten percent across the crust of a neutron star, it varies by less than a percent across the ocean, such that the assumption of constant g will modify the crust structure somewhat but will have very little effect on the ocean structure (for a given heat flux coming from the crust). As in BC09, we characterize the thermal conductivity in the inner crust with a single number, the impurity parameter $Q_{\text{imp}} = \langle Z^2 \rangle - \langle Z \rangle^2$. Our treatment of ϵ_{X_i} in the crust, as well as our treatment of ϵ across all layers, is described in Appendix C. In the ocean the components of b_i are found from the thermodynamic equations of Appendix D; K , c_P , and the other thermodynamic derivatives are found as in Paper I (see, e.g., equation 39 of that paper).

The ocean is bounded from above by the hydrogen and helium burning layer, which ends at a column depth y_0 . Rather than tracking the physics of this layer, we leave y_0 as a free parameter; in Sections 4 and 5 we choose $y_0 = 10^8 \text{ g cm}^{-2}$ (e.g., Bildsten & Brown 1997; cf. Fig. 2). The mass fraction of species i at the top of the ocean, $X_{i,0}$, is determined by the nuclear reactions within the burning layer (see Schatz et al. 2001). For the ^{16}O - ^{79}Se mixture described in Section 2 we nominally choose $\{X_{1,0}, X_{2,0}\} = \{0.02, 0.98\}$, as in Paper I (but see below). This is approximately the mixture the ocean would have if all of the light elements ($Z \leq 20$) were oxygen and all of the heavy elements ($Z > 20$) were selenium; further calculations, involving mixtures of more than two components, are required to determine whether this is a reasonable approximation.

The heavy-element ocean cannot penetrate into the light-element burning layer, such that the burning layer is stable to convection and the convective velocity drops to zero at the boundary [Eq. (B2)]. To include the stabilizing effect of this layer in our model we set

$$F_{r,X_i}(y_0) = 0 \quad (24)$$

and

$$F_{r,\text{conv}}(y_0) = 0. \quad (25)$$

The boundary conditions Eqs. (24) and (25) can occasionally be inconsistent with our assumption $X_{1,0} = 0.02$ above, in which case we allow $X_{1,0}$ to grow as necessary. Figure 2 shows an example of a case where $X_{1,0} > 0.02$ for our model (see also figure 3 from Paper II). Note that in the more accurate three-component model of Paper I there is no inconsistency between $F_{r,X_i}(y_0) = 0$ and $X_{1,0} = 0.02$, because the required rapid rise in X_{O} with increasing column depth is stabilized by the rapid drop in $X_{\text{H}} + X_{\text{He}}$. A similar situation occurs when convection is thermally driven ($\nabla \gtrsim \nabla_{\text{ad}}$ and $\sum_i \chi_i \nabla_{X_i} = 0$) at the top of the ocean.

The ocean is bounded from below by the crust, which

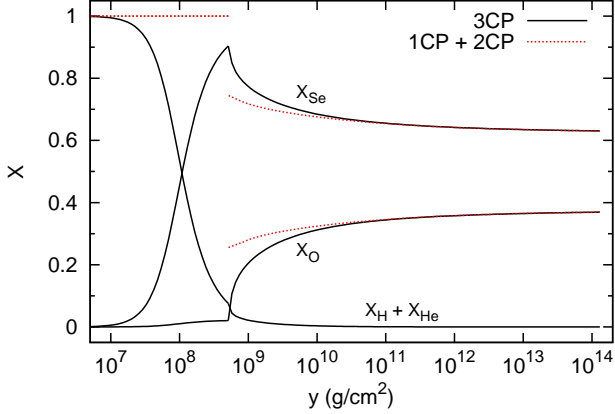


FIG. 2.— Composition profiles in an ^{16}O - ^{79}Se ocean and overlying hydrogen-helium burning layer. The hydrogen and helium are treated as a single component. The results from two models are shown: the three-component plasma (“3CP”) model from Paper I, where the burning layer and the ocean are allowed to mix through convection and nuclear reactions are included in a crude manner; and the one-component burning layer and two-component ocean (“1CP + 2CP”) model from this paper, where the two layers do not mix and nuclear reactions are included only in the sense that $\{X_i\}$ changes at the boundary ($y_0 = 5.1 \times 10^8 \text{ g/cm}^2$ for this example).

begins at a column depth y_b . The mass fraction of species i at the top of the crust, $X_{i,c}$, is determined by the mass fraction of species i at the base of the ocean, $X_{i,b}$, according to the relevant phase diagram. For ^{16}O - ^{79}Se we use Fig. 1 (see also Section 2.2); converting from number fraction to mass fraction gives

$$X_{1,c} = \begin{cases} X_{1,b}, & X_{1,b} \leq 0.01 \text{ or } X_{1,b} = 1; \\ 0.01 \text{ (“S2”)}, & 0.01 < X_{1,b} < 0.37; \\ 0.2 \text{ (“S1”)}, & 0.37 < X_{1,b} < 1 \end{cases} \quad (26)$$

for $\dot{y}_b < \dot{m}$, and

$$X_{1,c} = X_{1,b} \quad (27)$$

for $\dot{y}_b > \dot{m}$.

Convection can not occur for $y > y_b$, since the region is solid; therefore, at the ocean-crust boundary we set

$$F_{r,\text{conv}}(y_b^+) = 0, \quad (28)$$

where the superscript ‘+’ signifies that the flux is evaluated on the deep (i.e., crust) side of the boundary. The composition flux at the ocean base is

$$F_{r,X_i}(y_b^-) = (\dot{m} - \dot{y}_b)\Delta X_{i,bc}, \quad (29)$$

where $\Delta X_{i,bc} = X_{i,b} - X_{i,c}$ and the superscript ‘-’ signifies that the flux is evaluated on the shallow (i.e., ocean) side of the boundary [cf. the steady-state accretion expression $\dot{m}(X_{i,b} - X_{i,0})$ of Paper I]. If $\dot{y}_b \geq \dot{m}$, there will be no chemical separation at the boundary (Section 2.2) and therefore no compositionally driven convection in the ocean, such that

$$F_{r,X_i} = 0 \quad (30)$$

and

$$F_{r,\text{conv}} = 0 \quad (31)$$

throughout the ocean. Note that from Eqs. (26) and (29), $F_{r,X_1}(y_b^-) > 0$ for the O-Se system; with Eq. (17) this

means that $F_{r,\text{conv}}(y_b^-) < 0$ or that there is an inward heat flux at the base of the ocean due to compositionally driven convection (cf. Paper I).

We use a stationary grid for all column depths except y_b , which we track continuously. The rate at which the ocean-crust boundary moves is constrained by the heat flux continuity condition

$$F_{r,\text{cd}}(y_b^-) + F_{r,\text{conv}}(y_b^-) = F_{r,\text{cd}}(y_b^+), \quad (32)$$

which using Eqs. (17) and (29) becomes

$$\frac{c_P T_b (\dot{m} - \dot{y}_b) \chi_1}{\chi T} \left(1 + \frac{\chi T b_1}{\chi_1 c_P} \right) \left(1 - \frac{X_{1,c}}{X_{1,b}} \right) = F_{r,\text{cd}}(y_b^-) - F_{r,\text{cd}}(y_b^+). \quad (33)$$

To estimate $F_{r,\text{cd}}(y_b^-)$ and $F_{r,\text{cd}}(y_b^+)$ we use the temperature gradient between y_b and the nearest grid point on the low- y side and on the high- y side, respectively; for sufficiently small grid spacing this is a reasonable approximation. During rapid heating this approximation gives $F_{r,\text{cd}}(y_b^-) < F_{r,\text{cd}}(y_b^+)$ or $\dot{y}_b > \dot{m}$, such that to maintain self-consistency between Eqs. (31) and (32) we can not use Eq. (33) to find \dot{y}_b but must find y_b from Eq. (6).

In this paper we assume for simplicity that $\epsilon_{X_i} = 0$ in the ocean. In particular, this means that we ignore the effect of electron captures on the ocean composition. Therefore, using Eqs. (10) and (24), the composition flux at any point in the ocean satisfies

$$F_{r,X_i}(y) = \int_{y_0}^y \frac{\partial X_i(y')}{\partial t} dy' + \dot{m}(X_i - X_{i,0}). \quad (34)$$

From Eqs. (29) and (34) we have that the total change in ocean composition with time is given by

$$\int_{y_0}^{y_b} \frac{\partial X_i(y')}{\partial t} dy' = \dot{m}\Delta X_{i,0c} - \dot{y}_b\Delta X_{i,bc} \quad (35)$$

with $\Delta X_{i,0c} = X_{i,0} - X_{i,c}$; this expression is used as a consistency check when we solve for $\partial X_i/\partial t$ below. The first term in Eq. (35) represents the balance between the composition $\{X_{i,0}\}$ entering the ocean from the burning layer and the composition $\{X_{i,c}\}$ leaving the ocean to the crust, as driven by accretion; the second term represents the exchange of particles in the ocean to convert a solid block of composition $\{X_{i,c}\}$ into a liquid block of composition $\{X_{i,b}\}$, as the boundary moves inward (or vice versa as the boundary moves outward).

For the two-component ocean mixture considered in this paper, we solve for the evolution of the ocean composition and temperature structure as follows: In each time step we first guess a value for $\partial X_{1,b}/\partial t$. Our guess comes from the fact that composition changes slowly with depth near the base of the ocean, i.e., $\nabla_{X_1} = \chi T (\nabla_{\text{ad}} - \nabla)/\chi_1 \ll 1$; which with Eq. (35) gives the approximation

$$\frac{\partial X_{1,b}}{\partial t} \simeq \frac{\dot{m}\Delta X_{1,0c} - \dot{y}_b\Delta X_{1,bc}}{y_b}, \quad (36)$$

where \dot{y}_b is obtained from Eq. (33). Once $\partial X_{1,b}/\partial t$ is chosen, the update value $\hat{X}_{1,b}$ is found from

$$\hat{X}_{1,b} = X_{1,b} + \Delta t \frac{\partial X_{1,b}}{\partial t}, \quad (37)$$

where Δt is the current time step; \hat{X}_1 at every other depth in the ocean is found from $\hat{X}_{1,b}$ and Eq. (9), and then Eq. (37) is used to find $\partial X_1/\partial t$ at each depth. Finally, Eq. (34) is used with $\partial X_1/\partial t$ to find F_{r,X_1} for Eq. (18). The value of $\partial X_{1,b}/\partial t$ is modified and the procedure repeated until Eq. (35) holds true. The new value of T_b is found from $X_{1,b}$, y_b , and Eq. (6). We find that our initial guess, Eq. (36), often requires no extra iterations for reasonable accuracy.

From Eq. (35), the steady-state $\partial X_i/\partial t = 0$ is reached when $\dot{y}_b = 0$ and $\Delta X_{1,0c} = 0$; that is, when the ocean-crust boundary stops moving and, if accretion is ongoing, when the composition at the top of the ocean is the same as that at the top of the crust (cf. Paper I). The latter condition happens in our ^{16}O - ^{79}Se simulations when $X_{1,b} \simeq 0.37$ [see Eq. (26)] through a simple feedback mechanism: if $X_{1,b} < 0.37$ at the ocean base, $\Delta X_{1,0c} > 0$ (the crust has composition S2), such that $\partial X_1/\partial t > 0$ and $X_{1,b}$ rises above 0.37; if $X_{1,b} > 0.37$, $\Delta X_{1,0c} < 0$ (the crust has composition S1), such that $\partial X_1/\partial t < 0$ and $X_{1,b}$ drops below 0.37; the composition of the ocean base hovers around $X_{1,b} = 0.37$. In reality the eutectic nature of the phase diagram at $X_{1,b} = 0.37$ will most likely cause the ocean base to solidify in vertically lamellar sheets of alternating S1, S2 composition (e.g., Woodruff 1973).

4. CONVECTION DURING ACCRETION

Here we evolve an example O-Se ocean from quiescence to steady state after accretion turns on, using the time-dependent equations of Sections 2 and 3 and assuming that compositionally driven convection is active. For this example $\dot{m} = 10^5 \text{ g cm}^{-2} \text{ s}^{-1}$ ($\sim 1.1 \dot{m}_{\text{Edd}}$), $T_c = 10^8 \text{ K}$, $Q_{\text{imp}} = 0$, and $y_0 = 10^8 \text{ g cm}^{-2}$. For our initial conditions at the start of accretion we choose $T^{\text{init}} = T_c$ throughout the crust and ocean and $X_1^{\text{init}} = 0.01$ (i.e., “S2” in Fig. 1) throughout the ocean. The latter assumption is made because, even though $X_{1,b}$ can be large after a cooling episode, during the initial heating there is rapid inward movement of the ocean-crust boundary but no chemical separation, such that the bulk of the ocean has the same composition as the accreted crust (Section 2.2; but see Section 7).

Figure 3 shows the composition profile at various times during its evolution to steady state. The composition is shown only for the ocean; the top of the ocean is located at $y = 10^8 \text{ g cm}^{-2}$, while the base of the ocean is located at the rightmost extent of each curve and moves inward as $X_{1,b}$ increases. The top of the convection zone can also be seen in the figure, as the depth where X_1 reaches the burning layer level of 0.02 and flattens out.

Figure 4 shows the temperature profile at various times during its evolution to steady state. As is discussed in Section 2.2, the ocean moves through two regimes to reach steady state: Initially there is no compositionally driven convection, because of the strong accretion heating such that $\dot{y}_b > \dot{m}$; the temperature profile reaches a quasi-steady state that matches the steady-state profile in the case without convection (the red dotted curve in Fig. 4) in only a few years. Once that quasi-steady state is reached, $\dot{y}_b \ll \dot{m}$ and the system slowly evolves over hundreds of years to the final steady state (the black solid curve with $t_\infty = 490$ years).

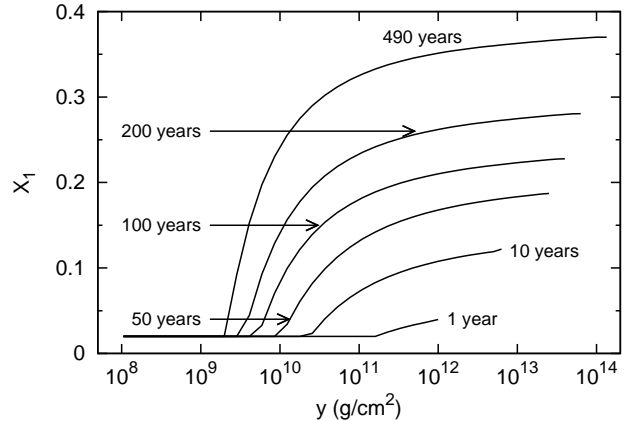


FIG. 3.— Composition profiles (in terms of the light element mass fraction X_1) in the ocean of a neutron star with compositionally driven convection, at various times after accretion turns on. Each curve is labeled with a t_∞ value; here t_∞ is the time from the start of the accretion outburst as seen by an observer at infinity. Steady state is reached at $t_{\infty,ss} = 490$ years, or $t_{ss} = t_{\infty,ss}/(1 + z_{\text{surf}}) = 370$ years.

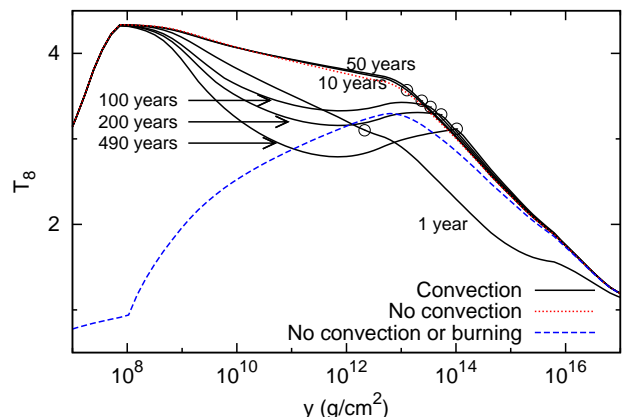


FIG. 4.— The temperature profile in the outer layers of a neutron star with compositionally driven convection, at various times after accretion turns on. The model parameters are the same as in Fig. 3. Each curve is labeled with a t_∞ value, and for each curve the location and temperature of the ocean-crust boundary is marked with an open circle. The temperature profiles for the cases without convection, and without convection or hydrogen and helium burning, are also plotted for comparison. Note that steady state for these latter cases is reached after only $t_\infty \simeq 15$ years.

While the ocean reaches the efficient convection state given by Eq. (9) relatively quickly, in approximately one convective turnover time $t_{\text{conv}} \sim 0.01 y_b / \dot{m}$ (months to a few years; see Paper I), it takes much longer to reach steady state, as can be seen in Figs. 3 and 4. The time from the start of the accretion outburst to the start of steady state can be estimated from Eq. (36): for a steady-state composition at the base of the ocean $X_{1,b}^{\text{ss}} = 0.37$ (Section 3), and a difference between the composition at the top of the ocean and the top of the crust $\Delta X_{1,0c} = 0.01$ [Eq. (26)], we have

$$t_{ss} \simeq \frac{X_{1,b}^{\text{ss}}}{\partial X_{1,b}/\partial t} \sim \frac{y_b}{\dot{m}} \frac{X_{1,b}^{\text{ss}}}{\Delta X_{1,0c}} \sim 1000 t_{\text{conv}} \quad (38)$$

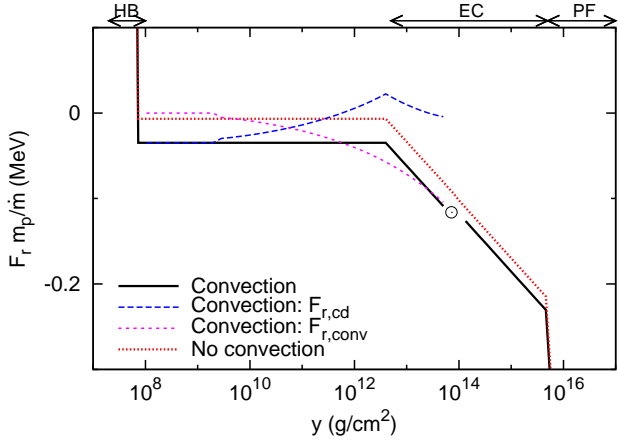


FIG. 5.— The total flux profile (in MeV nucleon^{-1}) in the outer layers of a neutron star with compositionally driven convection, in steady state and for the same parameters as in Fig. 3. The location and flux of the ocean-crust boundary is marked with an open circle; note also the gap at that point, where we chose not to plot the flux due to the discontinuity in the temperature derivative (Fig. 4). The labels that appear above the graph denote the column depths where the various accretion heat sources are active: HB is hydrogen and helium burning, EC is electron captures, and PF is pycnonuclear fusion (see Appendix C). The conduction ($F_{r,cd}$) and convection ($F_{r,conv}$) flux profiles, as well as the total flux profile for the case without convection, are also plotted for comparison.

(i.e., hundreds to thousands of years). Using Eq. (38) with $y_b \sim 10^{14} \text{ g cm}^{-2}$, we find a steady-state time of $t_{ss} \sim 10^3$ years (cf. Fig. 3). Note that if we instead use $\dot{m} \sim 10^4 \text{ g cm}^{-2} \text{ s}^{-1}$, as is typical for low-mass X-ray binaries, $t_{ss} \sim 10^4$ years. If $y_b \sim 10^{13} \text{ g cm}^{-2}$, as in the model of Horowitz et al. (2007) for $T_b \simeq 3 \times 10^8 \text{ K}$, the time to reach steady state is still large: $t_{ss} \sim 10^2$ years. If the mass fraction of light elements entering the ocean is ten times larger ($X_{1,0} \sim 0.2$), however, as is the case for stable hydrogen and helium burning (e.g., Stevens et al. 2014), $t_{ss} \sim y_b/\dot{m}$ is of order the accretion time.

Figure 5 shows the steady-state profiles for the total flux $F_r = F_{r,cd} + F_{r,conv}$ and the conduction and convection contributions. The convection contribution has a $y^{1/4}$ dependence, as in Eq. (21). At the top of the figure we have marked the locations of the three accretion heat sources considered in this paper: hydrogen and helium burning, electron captures, and pycnonuclear fusion (see Appendix C). Since in steady state $\partial F_r/\partial y \simeq -\epsilon$ [Eq. (23)], F_r is constant outside of the heat source regions and drops by $\int_{y_{low}}^{y_{high}} \epsilon dy$ across each region. For example, electron captures are active from a column depth of $y_{low} = 5 \times 10^{12} \text{ g cm}^{-2}$ to $y_{high} = 5 \times 10^{15} \text{ g cm}^{-2}$ and release a total energy of $Q_{EC} = (m_p/\dot{m}) \int_{y_{low}}^{y_{high}} \epsilon dy = 0.2 \text{ MeV nucleon}^{-1}$ (e.g., Haensel & Zdunik 2008), such that the total drop in $F_r m_p/\dot{m}$ over that range is 0.2 MeV.

Note that the results shown in Figs. 4 and 5 are qualitatively different from those in figure 6 of Paper I, despite the similarity in the parameters used. This is due to a simplification made in our earlier paper: F_{crust} , the outward radial heat flux coming from the crust, is not the same for a neutron star with compositionally driven convection as without. In reality, F_{crust} must be solved self-consistently with T_b ; because T_b is larger with con-

vection, less heat flows into the ocean from the crust and therefore F_{crust} is smaller (or more negative, as is the case in Fig. 5), which limits the growth of T_b (cf. figure 1 and discussion of Brown 2004). For the example of Fig. 4 the steady-state temperature at $y = 10^{14} \text{ g cm}^{-2}$ (near the ocean crust-boundary) is only 4% larger with convection than without; whereas for the model of Paper I it is 20% larger. The inclusion of hydrogen and helium burning has a comparable impact on our model, increasing the temperature at $y = 10^{14} \text{ g cm}^{-2}$ by 5% (compare the blue dashed curve and the red dotted curve in Fig. 4).

5. CONVECTION AFTER ACCRETION TURNS OFF

We now consider the evolution of the ocean as it cools in quiescence. We find that the evolution proceeds in four stages; these stages are discussed in detail in Paper II, but we outline them below for reference (cf. Figs. 6 and 7):

In stage 1, the base of the ocean has not yet started to cool and so the evolution is the same with or without convection. In stage 2, the cooling wave has reached the bottom of the ocean, and new crust begins to form, driving convection. Inward heat transport by convection rapidly cools the envelope and ocean but maintains the ocean-crust boundary at a nearly constant temperature and depth. The temperature gradient steepens with time. In stage 3, the temperature gradient at the base of the ocean ∇_b reaches $\nabla_L \simeq 0.25$, the liquidus temperature gradient. The region around the ocean-crust boundary alternates between a state of strong convective heating and crust melting, and a state of suppressed convection due to the release of heavy elements into the ocean. The sporadic convection can no longer prevent the ocean base from cooling, and cooling returns to a level similar to during stage 1. In stage 4, the crust is thermally relaxed, the ocean cools too slowly for convection to support the steep gradient $\nabla_b = \nabla_L$, and the temperature profile in the ocean flattens.

5.1. Analytic approximation

Here we present an analytic approximation to the model of Sections 2 and 3 applicable during cooling. In our approximation, we assume that the ocean thermal conductivity and the pressure scale height have the scaling relationships

$$K \propto y^{1/4} T \quad \text{and} \quad H_P \propto y^{1/4}, \quad (39)$$

respectively; these relationships are valid when the electrons are relativistic, i.e., for column depths around or greater than $y_t = 10^{10} \text{ g cm}^{-2}$. For each stage of cooling (see above or Paper II), we use Eq. (39) and a flux equation [Eq. (43) or (50)] to solve for the temperature T_t at depth y_t ; and then solve for the effective temperature T_{eff} using the approximate relation (cf. BC09)

$$\frac{d \ln T_{\text{eff}}}{d \ln T_t} \simeq 0.5, \quad (40)$$

or equivalently,

$$T_{\text{eff}} \simeq T_{\text{eff}}^{(s)} \left(\frac{T_t}{T_t^{(s)}} \right)^{1/2}, \quad (41)$$

where the superscript ‘(s)’ signifies that the quantity is evaluated at the beginning of stage s of cooling. To solve for the evolution of T_t we assume that the temperature profile through the ocean and crust has an initially constant gradient $\nabla^{(1)}$ (cf. Fig. 4; see also below). During cooling, there is a transition between the thermally relaxed outer layers with constant outward heat flux $\sigma_B T_{\text{eff}}^4$, where σ_B is the Stefan-Boltzmann constant, and the inner layers still in steady state with outward heat flux $KT\nabla^{(1)}/H_P$ [Eq. (13) with $\nabla = \nabla^{(1)}$]. While the cooling wave is still in the ocean, this transition is defined by the thermal time

$$\tau \simeq \frac{\rho c_P H_P^2}{2K} \propto y T^{-1} \quad (42)$$

(cf. Henyey & L’Ecuyer 1969); the factor of two in Eq. (42) comes from integrating equation 7 of BC09 assuming Eq. (39) for K and H_P and that c_P and T are constant. We define the transition depth y_τ as the depth where the thermal time is equal to the cooling time t .

During stage 1, the transition depth is above the base of the ocean, i.e., $y_\tau < y_b^{(1)}$, and there is no compositionally driven convection. The transition from the steady-state heat flux for $y > y_\tau$ to the surface heat flux $\sigma_B T_{\text{eff}}^4$ for $y \ll y_\tau$ is not sharp (see, e.g., the “20 days” curve of Fig. 6). For lack of a better model, and to maintain continuity between stages 1 and 2, we use a modified version of Eq. (50) for the heat flux: the (conductive) heat flux at any point $y \leq y_\tau$ is given by

$$\frac{KT}{H_P} \nabla = \left[\frac{KT}{H_P} \Big|_{y=y_\tau} \nabla^{(1)} - \sigma T_{\text{eff}}^4 \right] \left(\frac{y}{y_\tau} \right)^{5/4} + \sigma T_{\text{eff}}^4. \quad (43)$$

Here $Q|_{y=y_\tau}$ signifies that the quantity Q is evaluated at depth y_τ . Equation (43) has the desired properties of being continuous and giving the correct heat flux values in the limiting cases $y = y_\tau$ and $y \ll y_\tau$. With Eq. (39) we can solve Eq. (43) for the temperature profile through the ocean,

$$T = T_\tau \left[1 - \frac{8}{5} \left(\nabla^{(1)} - \nabla_{\text{eff},\tau} \right) \left\{ 1 - \left(\frac{y}{y_\tau} \right)^{5/4} \right\} + 2 \nabla_{\text{eff},\tau} \ln \left(\frac{y}{y_\tau} \right) \right]^{1/2}; \quad (44)$$

and the temperature at depth y_t near the top of the ocean,

$$T_t \simeq T_\tau \left[1 - \frac{8}{5} (\nabla^{(1)} - \nabla_{\text{eff},\tau}) + 2 \nabla_{\text{eff},\tau} \ln(y_t/y_\tau) \right]^{1/2}. \quad (45)$$

Here we assume $y_t \ll y_\tau$ and have defined

$$\sigma T_{\text{eff}}^4 \equiv \frac{KT}{H_P} \Big|_{y=y_\tau} \nabla_{\text{eff},\tau} \quad (46)$$

for convenience. From Eqs. (41) and (45) we obtain the

scaling relation

$$T_{\text{eff}} = T_{\text{eff}}^{(2)} \left(\frac{T_\tau}{T_\tau^{(2)}} \right)^{1/2} \times \left[\frac{1 - \frac{8}{5} \nabla^{(1)}}{1 - \frac{8}{5} \nabla^{(1)} + 2 \nabla_{\text{eff},\tau}^{(2)} \ln(y_\tau/y_\tau^{(2)})} \right]^{1/4}. \quad (47)$$

In deriving Eq. (47) we grouped T_{eff} terms and used the fact that $\nabla_{\text{eff},\tau} \propto T_{\text{eff}}^4/T_\tau^2$ [Eq. (46)].

To determine T_τ and y_τ as a function of time during stage 1, we use Eq. (42):

$$T_\tau = T_\tau^{(2)} \left(\frac{y_\tau}{y_\tau^{(2)}} \right)^{\nabla^{(1)}} = T_\tau^{(2)} \left(\frac{t}{t_2} \right)^{\nabla^{(1)/(1-\nabla^{(1)})}} \quad (48)$$

and therefore

$$y_\tau = y_\tau^{(2)} \left(\frac{t}{t_2} \right)^{1/(1-\nabla^{(1)})}, \quad (49)$$

where t_2 is the time at the beginning of stage 2 (see below). Along with $T_\tau^{(2)} = T_b^{(2)}$, $y_\tau^{(2)} = y_b^{(2)}$, and $\nabla_{\text{eff},\tau}^{(2)} = \nabla_{\text{eff}}^{(2)}$ [where ∇_{eff} is $\nabla_{\text{eff},\tau}$ taken at the base of the ocean; Eq. (53)], Eqs. (48) and (49) can be inserted into Eq. (47) to solve for T_{eff} during stage 1 (cf. equation 8 of BC09).

During stages 2 and 3, the ocean is thermally relaxed, such that the flux through the ocean satisfies $F_{r,\text{conv}} + F_{r,\text{cd}} = \sigma_B T_{\text{eff}}^4$. Since $F_{r,\text{conv}} \propto y^{5/4}$ [Paper I; see also Eq. (B8) with Eqs. (29) and (36)] and $F_{r,\text{cd}} = KT\nabla/H_P$, we have that the conductive flux in the ocean is given by

$$\frac{KT}{H_P} \nabla = \left[\frac{KT}{H_P} \Big|_{y=y_b} \nabla_b - \sigma T_{\text{eff}}^4 \right] \left(\frac{y}{y_b} \right)^{5/4} + \sigma T_{\text{eff}}^4. \quad (50)$$

Similar to our method for stage 1 above, we use Eq. (50) with Eq. (39) to solve for the temperature profile through the ocean,

$$T = T_b \left[1 - \frac{8}{5} (\nabla_b - \nabla_{\text{eff}}) \left\{ 1 - \left(\frac{y}{y_b} \right)^{5/4} \right\} + 2 \nabla_{\text{eff}} \ln \left(\frac{y}{y_b} \right) \right]^{1/2}, \quad (51)$$

and the temperature at depth y_t near the top of the ocean,

$$T_t \simeq T_b \left[1 - \frac{8}{5} (\nabla_b - \nabla_{\text{eff}}) + 2 \nabla_{\text{eff}} \ln(y_t/y_b) \right]^{1/2}, \quad (52)$$

where

$$\sigma T_{\text{eff}}^4 \equiv \frac{KT}{H_P} \Big|_{y=y_b} \nabla_{\text{eff}} \quad (53)$$

and we assume that $y_t \ll y_b$. From Eqs. (41) and (52)

we obtain the scaling relation

$$T_{\text{eff}} = T_{\text{eff}}^{(s)} \left(\frac{T_b}{T_b^{(s)}} \right)^{1/2} \times \left[\frac{1 - \frac{8}{5} \nabla_b}{1 - \frac{8}{5} \nabla_b^{(s)} + 2 \nabla_{\text{eff}}^{(s)} \ln(y_b/y_b^{(s)})} \right]^{1/4}. \quad (54)$$

In deriving Eq. (54) we grouped T_{eff} terms and used the fact that $\nabla_{\text{eff}} \propto T_{\text{eff}}^4/T_b^2$ [Eq. (53)].

Stage 2 begins at a time $t_2 = \tau_b^{(2)}$, where τ_b is the thermal time evaluated at the base of the ocean. At the beginning of this stage the ocean base is still in steady state, $\nabla_b^{(2)} = \nabla^{(1)}$. We assume that the transition depth is stationary, i.e., that $y_b = y_b^{(2)}$ and $T_b = T_b^{(2)}$ are constant. To determine ∇_b as a function of time we look at the ocean energetics: The total energy stored in the ocean is

$$E = A \int_{y_t}^{y_b} c_P T dy, \quad (55)$$

where A is the surface area; using Eq. (51) and assuming that c_P is constant in the ocean, that $y_t \ll y_b$, and that ∇_b and ∇_{eff} are small ($\nabla^{(1)} \leq \nabla_b \leq \nabla_L$ in this stage and $\nabla_{\text{eff}} \ll \nabla_{\text{ad}}$ typically), we have

$$E \simeq A c_P T_b y_b \left(1 - \frac{4}{9} \nabla_b - \frac{5}{9} \nabla_{\text{eff}} \right). \quad (56)$$

As ∇_b increases and the ocean cools, this energy is slowly depleted; using Eq. (56) and the fact that y_b and T_b are constant during stage 2, we have that the ocean energy changes at a rate

$$\frac{dE}{dt} \simeq -A c_P T_b y_b \left(\frac{4}{9} \frac{d\nabla_b}{dt} + \frac{5}{9} \frac{d\nabla_{\text{eff}}}{dt} \right), \quad (57)$$

The depleted energy is released at the ocean base and must mask the cooling due to the difference between the flux entering the ocean from the crust and the flux leaving the ocean through the top; i.e.,

$$-\frac{dE}{dt} = A \left. \frac{KT}{H_P} \right|_{y=y_b} (\nabla_{\text{eff}} - \nabla^{(1)}). \quad (58)$$

From Eq. (54) we have that

$$\frac{d\nabla_{\text{eff}}}{dt} = -\frac{8\nabla_{\text{eff}}^{(2)}}{5 \left(1 - \frac{8}{5} \nabla^{(1)} \right)} \frac{d\nabla_b}{dt}; \quad (59)$$

combining Eqs. (57)–(59) with $\nabla_{\text{eff}} \ll 1$ gives

$$\nabla_b \simeq \frac{9}{8} \left(\nabla_{\text{eff}}^{(2)} - \nabla^{(1)} \right) \left(\frac{t}{t_2} - 1 \right) + \nabla^{(1)}. \quad (60)$$

Along with $T_b = T_b^{(2)}$ and $y_b = y_b^{(2)}$, Eq. (60) can be inserted into Eq. (54) to solve for T_{eff} during stage 2.

Stage 3 begins when $\nabla_b = \nabla_L$, or at a time $t_3 = t_2 \left[8(\nabla_L - \nabla^{(1)})/9 \left(\nabla_{\text{eff}}^{(2)} - \nabla^{(1)} \right) + 1 \right]$. We assume that $\nabla_b = \nabla_L$ is constant. To determine T_b and y_b as a function of time during stage 3, we use Eq. (42) with c_P and K at their solid values such that $\tau \propto y^{3/4}$ (BC09): Because conduction is very efficient

at transporting heat in the crust, we assume that the temperature gradient in the crust from the ocean-crust boundary to the transition depth is flat (cf. Paper I); i.e., the ocean-crust boundary cools at the same rate as the transition depth, $\partial \ln T_b / \partial \ln t = \partial \ln T_\tau / \partial \ln t = (\partial \ln T_\tau / \partial \ln y_\tau)(\partial \ln y_\tau / \partial \ln \tau) = 4\nabla^{(1)}/3$, or equivalently,

$$T_b = T_b^{(3)} \left(\frac{t}{t_3} \right)^{4\nabla^{(1)}/3}. \quad (61)$$

If enrichment is low, $\partial \ln y_b / \partial t \simeq 4(\partial \ln T_b / \partial t)$ [Eq. (E10)], and we have

$$y_b \simeq y_b^{(3)} \left(\frac{t}{t_3} \right)^{16\nabla^{(1)}/3}; \quad (62)$$

but if enrichment is high (as is the case in Fig. 6; see figure 3 of Paper II), $\partial \ln y_b / \partial t \ll \partial \ln T_b / \partial t$, and we have

$$y_b \simeq y_b^{(3)}. \quad (63)$$

Along with $\nabla_b = \nabla_L$, $T_b^{(3)} = T_b^{(2)}$, and $y_b^{(3)} = y_b^{(2)}$, Eqs. (61)–(63) can be inserted into Eq. (54) to solve for T_{eff} during stage 3.

5.2. Results

Here we evolve the O-Se ocean from Section 4 as it cools after accretion turns off. For stages 1, 2, and 4 of cooling we use the equations from Sections 2 and 3, with $\dot{m} = 0$ and $\epsilon = 0$ as is appropriate during cooling. We can also use these equations for stage 3, but the resulting light curves are noisy unless the simulation time step and spatial resolution are very small, due to the quasi-periodic activation/deactivation of convection that occurs during this stage (see above). Instead, we use the following method, which has the advantage of requiring a much coarser time and spatial grid for (empirically) comparably smooth and accurate light curves: We assume that once compositionally driven convection is strong enough for $\nabla_b = \nabla_L$, it will remain at that critical level as cooling continues; i.e., we assume that when $\nabla_b \geq \nabla_L$,

$$F_{r,\text{conv}}(y_b^-) = F_{r,\text{cd}}(y_b^+) - \frac{KT_b}{H_P} \nabla_L \quad (64)$$

[cf. Eq. (32)]. Equation (33) can no longer be used to find \dot{y}_b , instead we use the ocean-crust boundary equations of Appendix E. From Eq. (E2) we have [cf. Eq. (6)]

$$\dot{y}_b = \frac{4y_b}{T_b} \frac{\partial T_b}{\partial t} + y_{b,1}' \frac{\partial X_{1,b}}{\partial t}, \quad (65)$$

where $y_{b,1}' = \partial y_b / \partial X_{1,b} - \partial y_b / \partial X_{2,b}$. We solve for $\partial T_b / \partial t$ using the entropy balance equation [Eq. (E7); cf. Eq. (11)]

$$T_b \frac{\partial s_b}{\partial t} - T_b \dot{y}_b \frac{\partial s}{\partial y} \Big|_{y=y_b^-} = \frac{\partial F_r}{\partial y} \Big|_{y=y_b} \quad (66)$$

$$\simeq \left[\frac{KT(\nabla_L - \nabla)}{H_P \Delta y} \right]_{y=y_b^-}, \quad (67)$$

where Δy is the grid spacing. Note that Eq. (67) drives the temperature gradient ∇_b to ∇_L . We solve for

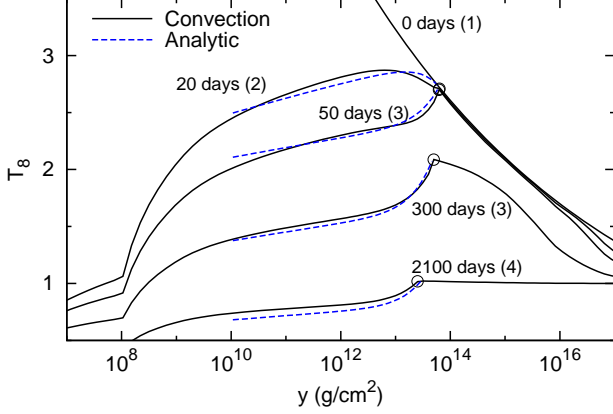


FIG. 6.— Temperature profiles in the outer layers of a neutron star with compositionally driven convection, and the analytic approximation to those profiles [Eq. (51)], at various times after accretion turns off. Each curve is labeled with a t_∞ value and the stage of cooling (see text) in parentheses; here t_∞ is the time from the start of the accretion outburst as seen by an observer at infinity. In addition, for each curve the location and temperature of the ocean-crust boundary is marked with an open circle. The parameters used for the analytic approximation are $\tau_b^{(2)} = 13.4$ days, $\nabla^{(1)} = -0.093$, and $\nabla_{\text{eff}}^{(2)} = 0.025$; such that stage 2 begins (to an outside observer) at $t_{2,\infty} = 17.6$ days and stage 3 begins at $t_{3,\infty} = 63.4$ days. We use T_b and y_b from the simulations, rather than from Eqs. (61)–(63), to obtain a better fit. (Cf. figure 2 of Paper II; note the typographical error in the “50 days” curve of that plot.)

$\partial X_{1,b}/\partial t$ using the iteration method described earlier, except that our initial guess is [Eq. (E9)]

$$\frac{\partial X_{1,b}}{\partial t} \simeq -\frac{4\Delta X_{1,bc}/T_b}{1 + y'_{b,1}\Delta X_{1,bc}/y_b} \frac{\partial T_b}{\partial t}. \quad (68)$$

We use the above method whenever $\nabla_b > \nabla_L$ (i.e., during stage 3), for all of the calculations shown here and in Section 6. Note that even with this method, the light curves are slightly noisy in stage 3 (see, e.g., Fig. 7).

In this section we choose initial conditions at the start of cooling $T^{\text{init}}(y = 10^{12} \text{ g cm}^{-2}) = 4 \times 10^8 \text{ K}$ near the base of the ocean, $T_c^{\text{init}} = 10^8 \text{ K}$ at the base of the crust, and a constant temperature gradient in between; and $X_{1,b}^{\text{init}} = 0.37$ at the base of the ocean with a composition profile given by Eq. (9) throughout the ocean. These are approximately the steady-state conditions from Section 4 (see also BC09; Paper II). Note that our assumption of an initially constant temperature gradient in the ocean and crust means that the convective flux is zero at the start of cooling, which is not entirely consistent with the steady-state results of Section 4. Our intent here is to show the effects of compositionally driven convection on cooling only. In Section 6 we run our simulations over an entire accretion cycle from outburst to quiescence, such that the convective fluxes during cooling are calculated in a self-consistent way.

Figure 6 shows the temperature profiles at various times during cooling, along with the analytic approximation to these profiles. As can be seen in the figure, the ocean-crust boundary moves outward more quickly during cooling than during accretion: Equation (33) as

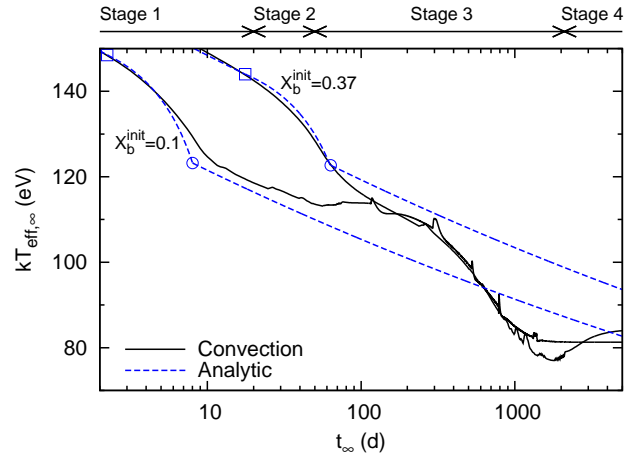


FIG. 7.— The cooling light curve of a neutron star with $X_b^{\text{init}} = 0.37$ and compositionally driven convection, and the analytic approximation to this light curve [Eqs. (47) and (54)]. Here t_∞ is the time from the end of the accretion outburst and $T_{\text{eff},\infty}$ is the effective temperature as seen by an observer at infinity. The labels that appear above the graph denote the duration of the stages of cooling (see text). For the analytic approximation, the transition from stage 1 to 2 and the transition from stage 2 to 3 are marked with an open square and an open circle, respectively. The parameters used are the same as in Fig. 6, with the addition of $y_b^{(2)} = 6.05 \times 10^{13} \text{ g cm}^{-2}$ and $T_b^{(2)} = 2.73 \times 10^8 \text{ K}$. The light curve and analytic approximation for the case with $X_b^{\text{init}} = 0.1$ are also plotted for comparison. (Cf. figure 1 of Paper II.)

it applies to the cooling case is given by

$$\dot{y}_b = -\frac{1}{\chi_1/\chi_T + b_1/c_P} \frac{X_{1,b}}{\Delta X_{1,bc}} \frac{F_{r,\text{cd}}(y_b^-) - F_{r,\text{cd}}(y_b^+)}{c_P T_b}; \quad (69)$$

using Eq. (13) with a temperature gradient at the ocean base $\nabla_b \sim 0.25$ (see below), we find $\dot{y}_b \sim -10^5 \text{ g cm}^{-2} \text{ s}^{-1}$. This is markedly different from the situation in Section 4, where $|\dot{y}_b| \ll \dot{m}$ over most of the evolution. The composition also evolves more quickly during cooling than during accretion: From Eq. (36) we have $\partial X_{1,b}/\partial t \simeq -\dot{y}_b \Delta X_{1,bc}/y_b$, which is a factor of $\sim \Delta X_{1,bc}/\Delta X_{1,0c} \gtrsim 20$ times larger than the accretion value [cf. Eq. (38)].

Figure 7 shows the cooling light curve along with the analytic approximation. As can be seen in the figure, changing $X_{1,b}^{\text{init}}$ has a strong effect on the light curve. This is for two reasons: First, for a larger light-element fraction in the ocean the thermal conductivity $K \propto \langle Z \rangle^{-1}$ is also larger; a larger K reduces the temperature gradient in the ocean (while self-consistently increasing the flux there), which keeps the outer layers hotter both during steady-state accretion and at the end of cooling when the crust and core are equilibrated (see BC09). Second, for a larger light-element fraction in the ocean the ocean-crust boundary is deeper, which delays the onset of strong ocean cooling due to compositionally driven convection. Note that in Fig. 7 the analytic approximation deviates strongly from the model light curve for $t_\infty \gtrsim 100$ days. This is because our analytic expressions [Eqs. (47) and (54)] only account for cooling of the ocean and crust by heat conduction out through the envelope, not for late-time cooling by heat conduction into the core (cf. BC09).

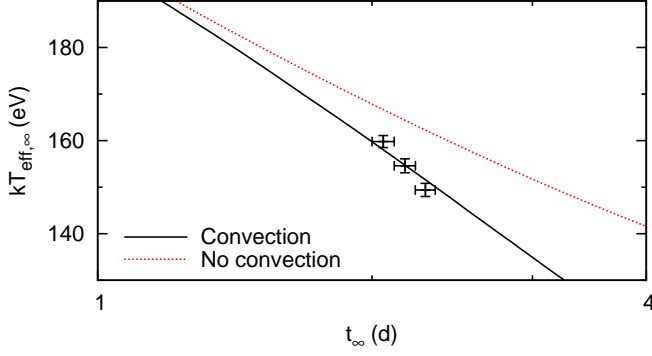


FIG. 8.— Model light curves with compositionally driven convection (solid curve) and without (dotted curve), plotted over the observations of XTE J1709–267. The solid curve is a fit to the observations, while the dotted curve has the same parameters as the solid curve. In our fit we assume that the first observation was taken 2 days after accretion turned off. We use $y_0 = 10^{10} \text{ g cm}^{-2}$, $T_c = 10^7 \text{ K}$, $Q_{\text{imp}} = 0$, and $X_{1,b}^{\text{init}} = 0.03$.

6. COMPARISON TO OBSERVATIONS

In Paper II we presented fits to observations of XTE J1701–462 and IGR J17480–2446, using our model of compositionally driven convection; here we present fits to observations of several additional quiescent, transiently accreting neutron stars. Our goal in making these fits was to understand qualitatively how including convection in the ocean changes the fitting parameters for these sources. Therefore, we did not attempt to accurately fit our model to the observational data using rigorous parameter searches. Similar to BC09, each source was fit by running our simulations from the onset of accretion through the duration of the accretion outburst, then turning off accretion and tracking the cooling light curve out to the end of the observation. In our fits we take \dot{m} and the duration of the accretion outburst from observations and fit to the parameters T_c , Q_{imp} , y_0 , and $X_{1,b}^{\text{init}}$. Note that in Degenaar et al. (2014) we assumed shallow heating in our fit of EXO 0748–676 (see also BC09). In this paper we do not include shallow heating in our model directly. Instead, we vary y_0 to provide the necessary shallow heating, with a larger y_0 placing the burning layer closer to the bulk of the ocean and heating it more.

Figures 8 and 9 (see also figure 4 of Paper II) show our fits to cooling light curves from several quiescent sources. Note that in most of our fits we use $y_0 \sim 10$ times larger than the standard value of a few $\times 10^8 \text{ g cm}^{-2}$ (e.g., Bildsten & Brown 1997; Paper I); i.e., we must invoke a significant shallow heat source. Convection does not directly reduce the required shallow heat source for each fit: For the same shallow heating (same values of y_0) the fits for our model with and without convection are generally equally valid (e.g., in Fig. 9); in addition, the fitted ocean temperature at the start of cooling is similar in both our model and that of BC09, implying the use of a comparable shallow heating model. Instead, convection justifies the use of larger values of $X_{1,b}$ in our models due to light-element enrichment, which in turn increases the thermal conductivity in the ocean and makes it hotter without the need for shallow heating (see, e.g., the effect of different $X_{1,b}^{\text{init}}$ values in Fig. 7).

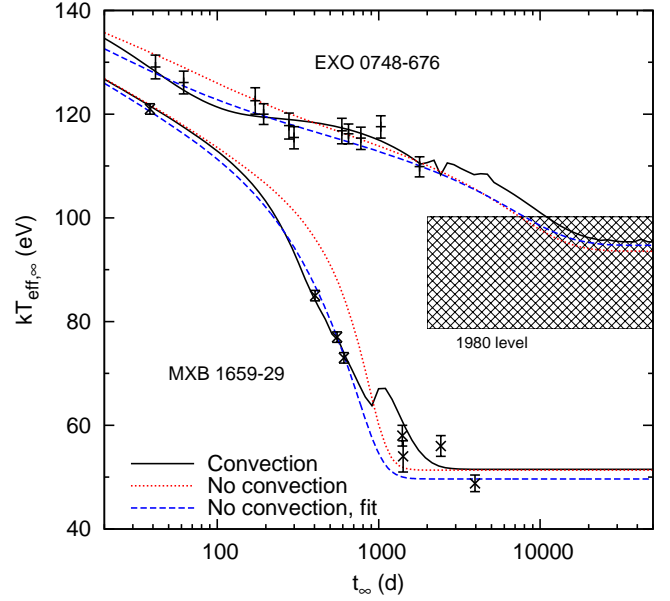


FIG. 9.— Model light curves with compositionally driven convection (solid curves) and without (dashed and dotted curves), plotted over the observations of EXO 0748–676 and MXB 1659–29. For each source, the solid curve and the dashed curve are fits to the observations, while the dotted curve has the same parameters as the solid curve. For EXO 0748–676, the pre-outburst data ($kT_{\text{eff},\infty} = 94.6^{+5.6}_{-16.0} \text{ eV}$) is marked with a shaded bar. For EXO 0748–676 we set $y_0 = 6 \times 10^9 \text{ g cm}^{-2}$ and $Q_{\text{imp}} = 40$, and use $T_c = 1.15 \times 10^8 \text{ K}$ and $X_{1,b}^{\text{init}} = 0.4$ (solid and dotted curves) and $T_c = 1.2 \times 10^8 \text{ K}$ and $X_{1,b}^{\text{init}} = 0.3$ (dashed curve) (cf. Degenaar et al. 2014). For MXB 1659–29 we set $y_0 = 10^9 \text{ g cm}^{-2}$ and $T_c = 3 \times 10^7 \text{ K}$, and use $Q_{\text{imp}} = 4$ and $X_{1,b}^{\text{init}} = 0.8$ (solid and dotted curves) and $Q_{\text{imp}} = 5$ and $X_{1,b}^{\text{init}} = 0.55$ (dashed curve). The late-time wiggles in the EXO 0748–676 convection curve (from $t_\infty \simeq 2000$ to 9000 days post-outburst) are numerical artifacts; however, the bump in the MXB 1659–29 convection curve (at $\simeq 1000$ days) is physical, caused by light-element saturation in the ocean as described in the text.

In our fits here and in Paper II, several trends appear when comparing the light curve from the model with compositionally driven convection to that from the model without convection, for the same parameters (see also Fig. 7). First, at $t_\infty \sim 1$ –100 days post-outburst the light curve with convection drops below the light curve without convection then flattens out, as the cooling transitions from stage 1 to stage 2 to stage 3 (Section 5). This arises because the compositionally-driven convection transports heat inwards, rapidly cooling the ocean and temporarily slowing the cooling in the crustal layers where the phase separation occurs. Second, at late times the light curve with convection crosses above the light curve without convection, due to light-element enrichment during convection increasing the ocean thermal conductivity (stage 4); for several of our fits (IGR J17480–2446 from Paper II, EXO 0748–676, and MXB 1659–29) this happens within the observation. Third, our fits that have steep (shallow) light curves with convection will have correspondingly steep (shallow) light curves without convection; compare, e.g., our fits for MXB 1659–29 versus those for EXO 0748–676 in Fig. 9. This is because, whether or not compositionally driven convection is in effect, the crust ultimately drives the cooling (see Section 5). We do not discuss the

behavior of the crust cooling in this paper; a detailed discussion can be found in BC09.

As can be seen from Figs. 8 and 9, we generally fit currently available light curves equally well with and without compositionally driven convection. Detecting the signature of convection will require better sampling of the early phase of the cooling curve. XTE J1709–267 ($\dot{m} = 2 \times 10^4 \text{ g cm}^{-2} \text{ s}^{-1}$ with a 10 week outburst; Degenaar et al. 2013b) is the exception to the above generalization, since the model with convection fits better to the observed rapid decrease in the cooling light curve (Fig. 8; cf. stage 2 of Fig. 7). Convection also provides an explanation for the observed increase in the equilibrium flux level in IGR J17480–2446 from 2009 to 2014 (Degenaar et al. 2013a; see Paper II), because it allows the composition, and therefore the equilibrium temperature profile, to change from one accretion episode to the next. For XTE J1701–462 (Fridriksson et al. 2011; see Paper II), we find that with convection we can match the drop in the light curve at 100–200 days (Fig. 10). Similarly for EXO 0748–676 ($\dot{m} = 2 \times 10^3 \text{ g cm}^{-2} \text{ s}^{-1}$ with a 24 year outburst; Degenaar et al. 2011, 2014), we find that the inclusion of convection leads to a plateau of slow cooling between $\simeq 150$ –750 days post-outburst, broadly consistent with the data (Fig. 9). We note that the model with convection is not statistically preferred over the model without convection.

BC09 fit the light curve of MXB 1659–29 ($\dot{m} = 9 \times 10^3 \text{ g cm}^{-2} \text{ s}^{-1}$ with a 2.5 year outburst; Wijnands et al. 2003, 2004; Cackett et al. 2008, 2013) with a standard cooling model. Using similar parameters and including convection gives a model light curve with a “stage 2” drop at ~ 50 days. Because of the gap in the data at $\simeq 40$ –400 days, we have the freedom in our fits to choose where this drop occurs; we can instead move the drop to ~ 200 days by increasing $X_{1,b}^{\text{init}}$ to an unphysical 0.8 (but see below). Note that in our model there is an abrupt jump in the light curve at late time ($t_\infty \simeq 1000$ days in Fig. 9), where the base of the ocean is saturated with light elements and compositionally driven convection halts (Section 5). This is a general feature of our fits to MXB 1659–29, as long as $X_{1,b}^{\text{init}} \gtrsim 0.3$, and it arises due to the steep drop in the light curve which causes rapid and prolonged outward motion of the ocean-crust boundary and strong chemical separation ($X_{1,b} \rightarrow 1$). The observations at late times neither support nor dispute the existence of this predicted bump (see Fig. 9).

With the model of Sections 2 and 3 it is impossible to fit both “anomalous” data points in the light curve of XTE J1701–462 (the two points from $t_\infty \simeq 200$ to 300 days post-outburst in Fig. 10; see also figure 4 of Paper II). However, we can partially fit this data by considering ocean mixtures other than oxygen-selenium and/or large values of $X_{1,b}^{\text{init}}$. Two such fits, one for a calcium-selenium ocean and one for an iron-selenium ocean (cf. Horowitz et al. 2007), are shown in Fig. 10; here the light-element saturation in the ocean produces a bump in the light curve that matches the second anomalous data point and that has a peak occurring at the same time as the first anomalous data point. We believe these modifications to our basic model to be reasonable, considering our uncertainty regarding what two-component mixture to use for the ocean or whether a two-component

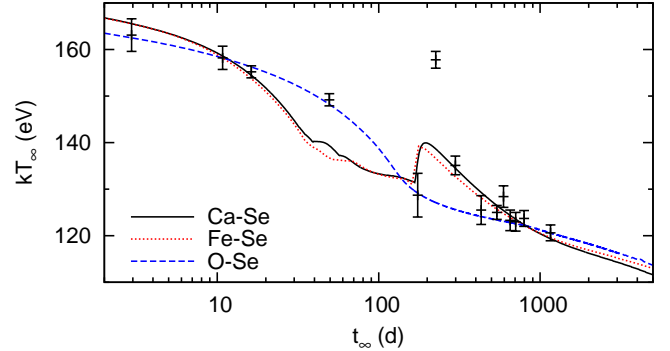


FIG. 10.— Model light curves with compositionally driven convection, plotted over the observations of XTE J1701–462. Here we deviate from the model of Sections 2 and 3 by using an ocean mixture of Ca-Se (solid line) and Fe-Se (dotted line), in place of O-Se (dashed line). For the Ca-Se ocean we use $y_0 = 10^8 \text{ g cm}^{-2}$, $T_c = 1.7 \times 10^8 \text{ K}$, $Q_{\text{imp}} = 200$, and $X_{1,b}^{\text{init}} = 0.5$; for the Fe-Se ocean we use $y_0 = 10^8 \text{ g cm}^{-2}$, $T_c = 2 \times 10^8 \text{ K}$, $Q_{\text{imp}} = 200$, and $X_{1,b}^{\text{init}} = 0.74$; and for the O-Se ocean we use the parameters from Paper II, $y_0 = 5 \times 10^7 \text{ g cm}^{-2}$, $T_c = 1.8 \times 10^8 \text{ K}$, $Q_{\text{imp}} = 40$, and $X_{1,b}^{\text{init}} = 0.37$. The bumps in the Ca-Se and Fe-Se curves are caused by light-element saturation in the ocean.

mixture is an accurate representation of the ocean. The large changes produced in the light curves when different compositions are used (figure 4 of Paper II vs. Fig. 10) emphasizes the need for models with three or more components. In addition, as we discuss in Section 7, it may be possible to reproduce the amplitude of the rebrightening in XTE J1701–462 by including heating due to electron captures self-consistently in our convection model.

7. DISCUSSION

In this paper we have continued the exploration begun in Paper I of the consequences of chemical separation and subsequent compositionally driven convection in the ocean of accreting neutron stars; while the model described in Paper I included only a steady-state ocean, here we use a full envelope-ocean-crust model and track its behavior from the onset of accretion to the end of cooling.

We have discovered a strong effect due to compositionally driven convection on the light curves of cooling, transiently accreting neutron stars. As the neutron star cools after an accretion outburst, the ocean-crust boundary moves outward. We find that this leads to chemical separation, and then convective mixing and inward heat transport, in a manner similar to that during accretion but at a much faster rate. The inward heat transport cools the outer layers of the ocean rapidly, but keeps the inner layers hot; the result is a sharp drop in surface emission at around a week (depending on parameters), followed by a gradual recovery as the ocean base moves outward. Such a dip should be observable in the light curves of these neutron star transients, if enough data is taken at a few days to a month after the end of accretion. If such a dip is definitively observed, it will provide strong constraints on the chemical composition of the ocean and outer crust.

Enrichment of the ocean with carbon remains a major issue for superburst models (Schatz et al. 2003). Following Horowitz et al. (2007) and Paper I, we chose oxygen

as the light element for our examples in this paper, but we have calculated models with carbon as the light element with similar results (as expected, due to the comparable heavy-element-to-light-element charge ratios and mass numbers of the C-Se and O-Se systems which yield comparable phase diagrams and thermodynamic quantities). We find that chemical separation can enrich the ocean to the required carbon fraction $X_{C,\text{ign}} \simeq 0.1$ (Schatz et al. 2003) within a few months of cooling after an accretion outburst (cf. Section 5). This is well within the estimated superburst recurrence time of 1–3 years (Kuulkers 2002; in ’t Zand et al. 2003), and is far more efficient than either chemical separation during accretion heating or gravitational sedimentation during quiescence. The rapid enrichment during cooling may help explain the puzzling superburst observed immediately before the onset of an accretion outburst in EXO 1745–248 (Altamirano et al. 2012): since the carbon in the ocean is at the required ignition level before accretion even starts, if the ocean can be heated strongly enough with a small amount of accretion a superburst can occur right at the beginning of an outburst.

In order for chemical separation to occur, however, the composition at the base of the ocean and at the top of the crust must differ; this will not happen if accretion outbursts are too short to push accreted material to the base of the ocean. Ultimately the carbon excess is being supplied by the ashes of the hydrogen and helium burning layer, with carbon mass fraction $X_{C,0} \lesssim 0.01$ during unstable burning (Woosley et al. 2004). This excess is driven to the ignition depth $y_{\text{ign}} \sim 10^{12} \text{ g cm}^{-2}$ within a few months to a year (y_{ign}/\dot{m}); but it takes ten times longer to build the excess up to the required fraction 0.1 (cf. Fig. 3). The total build-up time is at best a factor of three longer than the estimated superburst recurrence time of 1–3 years (Kuulkers 2002; in ’t Zand et al. 2003). We suggest that while a recurrence rate of a few years can not be sustained through compositionally driven convection, it is possible to have several bursts in a row at that rate if a small fraction of carbon can be “stored” in the deep ocean or crust (perhaps in lamellar sheets; see Section 3) after each burst. On the other hand, in ’t Zand et al. (2003) inferred observationally that stable burning is happening in superburst sources. Although the physical mechanism for the stable burning is not understood, it could produce much larger carbon fractions $X_{C,0} \sim 0.2$ (Stevens et al. 2014), which would reduce the timescale needed to enrich the ocean even during accretion (Section 4).

Note that while compositionally driven convection may help superburst models reach the levels of carbon enrichment required for carbon ignition, it does not help the models reach the required large ocean temperatures $T_{\text{ign}} \sim 6 \times 10^8 \text{ K}$ (Cumming et al. 2006). In fact, we find (Sections 4 and 5) that temperatures in the bulk of the

ocean are slightly lower with convection than without.

Two issues presented in Paper I have been resolved in the Appendix of this paper. In Appendix B we discuss what happens when $\nabla > \nabla_{\text{ad}}$ in the ocean (see also Section 3). As we alluded to in Paper I, the small amount of hydrogen and helium in the transition region between the burning layer and the ocean stabilize the density gradient at the top of the ocean and allows for an unstable temperature gradient and heavy-element composition gradient simultaneously, such that there is no contradiction between a small convective velocity at the top of the ocean and a smooth composition transition from the burning layer to the ocean. In Appendix F we discuss how rotation and magnetic fields affect our model. We find that the efficient convection assumption Eq. (9) remains valid even in the presence of rapid rotation and moderate magnetic fields; the remaining temperature and composition evolution equations in the paper follow directly from it and are therefore also unaffected by rotation or magnetic field.

There remains much to be explored theoretically. We have included only two species in our calculations, oxygen and selenium, which approximates the rp-process ashes used by Horowitz et al. (2007). The phase diagram for multicomponent mixtures is complex but can be calculated (Horowitz et al. 2007; Medin & Cumming 2010) and should be included. Multiple, consecutive, accretion outburst-quiescence cycles should also be simulated to obtain self-consistent composition profiles in the ocean and outer crust. It will be important to include carbon burning in the models.

We have assumed that solid particles form at a single depth. However, electron capture reactions may occur in the ocean (e.g., ^{56}Fe captures at a density of $1.5 \times 10^9 \text{ g cm}^{-3}$; Haensel & Zdunik 1990), lowering the $\langle Z \rangle$ at that depth, and potentially leading to formation of solid particles pre-electron capture above the post-electron capture liquid layers. The heat released due to electron captures during mixing and sedimentation of the region could be observable in the light curve. Further work is needed to understand how electron captures would affect the model presented here.

We thank Chuck Horowitz, Nathalie Degenaar, and Chris Fontes for useful discussions. Z.M. was supported by a LANL Director’s Postdoctoral Fellowship. A.C. is supported by an NSERC Discovery grant, and is a member of the Centre de Recherche en Astrophysique du Québec (CRAQ) and an Associate of the CIFAR Cosmology and Gravity program. This research was carried out in part under the auspices of the National Nuclear Security Administration of the U.S. Department of Energy at Los Alamos National Laboratory and supported by Contract No. DE-AC52-06NA25396.

APPENDIX

CONVECTIVE STABILITY

Here we derive expressions for the convective discriminant \mathcal{A} and other quantities related to entropy production and convective stability in the multicomponent oceans of neutron stars.

The usual stability requirement for a displaced fluid element is (e.g., Kippenhahn & Weigert 1994)

$$\mathcal{A} < 0, \tag{A1}$$

where

$$\mathcal{A} = \frac{d \ln \rho}{dr} - \left(\frac{d \ln \rho}{dr} \right)_{s, X_i, Y_e} \quad (\text{A2})$$

with d/dr the gradient in the star and $(d/dr)_{s, X_i, Y_e}$ the gradient felt by an element displaced at constant entropy s and chemical composition $\{X_i, Y_e\}$ (i.e., we assume the element is displaced with no radiated energy and no chemical diffusion). In the neutron star ocean, the sound speed is much larger than the convective velocity, such that a displaced element is always in pressure balance with its surroundings:

$$\frac{d \ln P}{dr} = \left(\frac{d \ln P}{dr} \right)_{s, X_i, Y_e} . \quad (\text{A3})$$

Using Eq. (A3) and

$$d \ln P = \chi_T d \ln T + \chi_\rho d \ln \rho + \sum_{i=1}^n \chi_{X_i} d \ln X_i + \chi_{Y_e} d \ln Y_e , \quad (\text{A4})$$

we can rewrite \mathcal{A} as

$$\mathcal{A} = -\frac{1}{\chi_\rho} \left[\chi_T \frac{d \ln T}{dr} + \sum_{i=1}^n \chi_{X_i} \frac{d \ln X_i}{dr} + \chi_{Y_e} \frac{d \ln Y_e}{dr} - \chi_T \left(\frac{d \ln T}{dr} \right)_{s, X} \right] ; \quad (\text{A5})$$

defining

$$\chi_i = \chi_{X_i} - \chi_{X_n} \frac{X_i}{X_n} + \chi_{Y_e} \frac{(Y_i - Y_n) X_i}{Y_e} \quad (\text{A6})$$

and enforcing the constraints $\sum_{i=1}^n X_i = 1$ and $Y_e = \sum_{i=1}^n Y_i X_i$, the convective discriminant becomes

$$\mathcal{A} = \frac{1}{H_P \chi_\rho} \left[\chi_T (\nabla - \nabla_{\text{ad}}) + \sum_{i=1}^{n-1} \chi_i \nabla X_i \right] . \quad (\text{A7})$$

Using

$$\left(\frac{\partial s}{\partial T} \right)_{P, X_i, Y_e} = \frac{c_P}{T} , \quad (\text{A8})$$

$$\left(\frac{\partial s}{\partial P} \right)_{T, X_i, Y_e} = - \left(\frac{\partial T}{\partial P} \right)_{s, X_i, Y_e} \left(\frac{\partial s}{\partial T} \right)_{P, X_i, Y_e} = - \frac{\nabla_{\text{ad}}}{P} c_P , \quad (\text{A9})$$

and Eqs. (D7) and (D8), we have

$$ds = c_P d \ln T - c_P \nabla_{\text{ad}} d \ln P - \sum_{i=1}^n b_{P,i} d \ln X_i - b_{P,e} d \ln Y_e ; \quad (\text{A10})$$

defining

$$b_i = b_{P,i} - b_{P,n} \frac{X_i}{X_n} + b_{P,e} \frac{(Y_i - Y_n) X_i}{Y_e} \quad (\text{A11})$$

and again enforcing $\sum_{i=1}^n X_i = 1$ and $Y_e = \sum_{i=1}^n Y_i X_i$, we can rewrite Eq. (A10) as

$$ds = c_P d \ln T - c_P \nabla_{\text{ad}} d \ln P - \sum_{i=1}^{n-1} b_i d \ln X_i . \quad (\text{A12})$$

Therefore

$$\frac{ds}{dr} = -\frac{1}{H_P} \left[c_P (\nabla - \nabla_{\text{ad}}) - \sum_{i=1}^{n-1} b_i \nabla X_i \right] . \quad (\text{A13})$$

Assuming that the pressure at a given depth does not change with time (cf. appendix A of Brown & Bildsten 1998) we also have from Eq. (A12) that

$$\frac{\partial s}{\partial t} = \frac{c_P}{T} \frac{\partial T}{\partial t} - \sum_{i=1}^{n-1} \frac{b_i}{X_i} \frac{\partial X_i}{\partial t} . \quad (\text{A14})$$

MIXING LENGTH EQUATIONS AND EFFICIENT CONVECTION

Here we derive or define expressions for several quantities related to heat transfer and composition mixing, first using mixing length theory and then using the efficient convection assumption of Eq. (9). We discuss the regimes in which either model is appropriate. Finally we discuss how to make these models consistent with an ocean that has $\nabla > \nabla_{\text{ad}}$.

In mixing length theory (e.g., Kippenhahn & Weigert 1994), a displaced element feels an average force per unit mass of

$$-\frac{gD\rho}{2\rho} = -\frac{g}{2\rho} \left[\left(\frac{d\rho}{dr} \right)_{s, X_i, Y_e} - \frac{d\rho}{dr} \right] = \frac{1}{2} g \mathcal{A} l_m \quad (\text{B1})$$

applied over an average distance of $l_m/2$; assuming that approximately half of this work goes into the kinetic energy of the particle, the convective velocity is given by

$$v_{\text{conv}}^2 = c_s^2 \frac{\xi^2}{8\chi_\rho} \left(\chi_T (\nabla - \nabla_{\text{ad}}) + \sum_{i=1}^{n-1} \chi_i \nabla_{X_i} \right) = \frac{1}{8} g \mathcal{A} l_m^2 \quad (\text{B2})$$

where $c_s = (gH_P)^{1/2}$ is the sound speed and $\xi = l_m/H_P$ is the ratio between the convection mixing length l_m and the scale height (but see Appendix F). The composition flux for species i is given by

$$F_{r, X_i} \hat{\mathbf{r}} = \rho v_{\text{conv}} D X_i \hat{\mathbf{r}} \quad (\text{B3})$$

where the composition “excess” of the displaced element over its surroundings is

$$D X_i = -\frac{l_m}{2} \frac{dX_i}{dr} = \frac{\xi}{2} X_i \nabla_{X_i}; \quad (\text{B4})$$

the convective heat flux is given by

$$F_{r, \text{conv}} \hat{\mathbf{r}} = \rho v_{\text{conv}} T D s \hat{\mathbf{r}} \quad (\text{B5})$$

where

$$D s = -\frac{l_m}{2} \frac{ds}{dr} = \frac{\xi}{2} c_P \left(\nabla - \nabla_{\text{ad}} - \frac{1}{c_P} \sum_{i=1}^{n-1} b_i \nabla_{X_i} \right) \quad (\text{B6})$$

using Eq. (A13). To solve for the evolution of the ocean using mixing length theory, we assume a value for ξ and use Eqs. (B2)–(B6) to find F_{r, X_i} and $F_{r, \text{conv}}$ for Eqs. (10) and (11).

For efficient convection [Eq. (9)], Eq. (A13) becomes

$$T \dot{m} \frac{\partial s}{\partial y} = -\frac{c_P T \dot{m}}{y} \sum_{i=1}^{n-1} \frac{\chi_i}{\chi_T} \left(1 + \frac{\chi_T b_i}{\chi_i c_P} \right) \nabla_{X_i}, \quad (\text{B7})$$

while Eq. (B5) with Eq. (B3) becomes

$$F_{r, \text{conv}} = -\frac{c_P T}{\chi_T} \sum_{i=1}^{n-1} \frac{\chi_i}{\chi_T} \left(1 + \frac{\chi_T b_i}{\chi_i c_P} \right) \frac{F_{r, X_i}}{X_i}. \quad (\text{B8})$$

Using Eqs. (10), (B7), and (B8) with $\epsilon_X = 0$, we have

$$\frac{\partial F_{r, \text{conv}}}{\partial y} = -\sum_{i=1}^{n-1} \left\{ \frac{c_P T \chi_i}{X_i \chi_T} \left(1 + \frac{\chi_T b_i}{\chi_i c_P} \right) \left[\frac{\partial X_i}{\partial t} + \dot{m} \frac{\partial X_i}{\partial y} \right] + F_{r, X_i} \frac{\partial}{\partial y} \left[\frac{c_P T \chi_i}{X_i \chi_T} \left(1 + \frac{\chi_T b_i}{\chi_i c_P} \right) \right] \right\}, \quad (\text{B9})$$

such that with Eqs. (12), (A14), and (B7) the energy balance equation Eq. (11) becomes

$$c_P \frac{\partial T}{\partial t} + \sum_{i=1}^{n-1} \frac{c_P T \chi_i}{X_i \chi_T} \frac{\partial X_i}{\partial t} = \frac{\partial F_{r, \text{cd}}}{\partial y} - \sum_{i=1}^{n-1} F_{r, X_i} \frac{\partial}{\partial y} \left[\frac{c_P T \chi_i}{X_i \chi_T} \left(1 + \frac{\chi_T b_i}{\chi_i c_P} \right) \right] + \epsilon. \quad (\text{B10})$$

To solve for the evolution of the ocean using the efficient convection assumption we use the procedure described in Section 3. Note that Eqs. (B7)–(B10) are independent of ξ , such that we do not need to assume a value for this parameter.

Figure 11 shows the composition profile for the example from Section 4, using mixing length theory with various values of ξ , and using the efficient convection assumption. The value of ξ at which efficient convection becomes a good approximation in the neutron star ocean can be estimated using Eq. (29) as an upper bound for the composition flux: Eq. (B3) gives

$$\frac{\xi}{2} \rho v_{\text{conv}, \text{max}} \simeq \frac{\dot{m} - \dot{y}_b}{\sum_{i=1}^{n-1} \chi_i \nabla_{X_i}} \sum_{i=1}^{n-1} \chi_i \frac{\Delta X_{i, bc}}{X_i} \sim 10^7 \text{ g cm}^{-2} \text{ s}^{-1}; \quad (\text{B11})$$

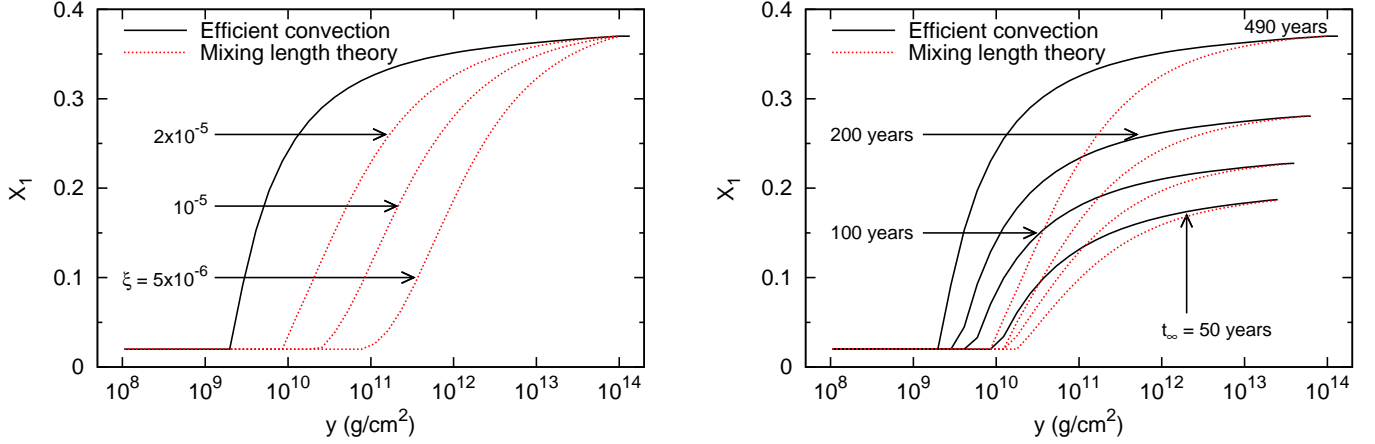


FIG. 11.— Composition profiles in the ocean of a neutron star with compositionally driven convection, in mixing length theory for various values of ξ and in the efficient convection assumption. The left panel shows the steady-state composition profiles as ξ increases from 5×10^{-6} to 2×10^{-5} ; the right panel shows the composition profile at various times for $\xi = 2 \times 10^{-5}$ and in the efficient convection assumption.

using Eq. (B2), $v_{\text{conv}} \leq v_{\text{conv,max}}$, and $\dot{m} - \dot{y}_b \sim 10^5 \text{ g cm}^{-2} \text{ s}^{-1}$ we have

$$\frac{\sum_{i=1}^{n-1} \chi_i \nabla X_i}{\chi_T (\nabla_{\text{ad}} - \nabla)} - 1 \leq \frac{32 \chi_\rho}{\xi^4} \left(\frac{\frac{\xi}{2} \rho v_{\text{conv,max}}}{\rho c_s} \right)^2 \sim \left(\frac{10^{-5}}{\xi} \right)^4. \quad (\text{B12})$$

This means that for mixing length parameters $\xi \gg 10^{-5}$ (as we assumed in Paper I), convection is efficient; i.e., $\sum_{i=1}^{n-1} \chi_i \nabla X_i$ is extremely close to its maximum stable value, $\chi_T (\nabla_{\text{ad}} - \nabla)$. Note that when $\xi \gg 10^{-5}$, small numerical errors in $\chi_T (\nabla - \nabla_{\text{ad}}) + \sum_{i=1}^{n-1} \chi_i \nabla X_i$ lead to very large errors in v_{conv} . In this case we can not use the full mixing length procedure but must assume efficient convection.

In Paper I we suggested that a time-dependent calculation could help resolve what happens when a stable composition profile can not extend from the burning layer ash at the top of the ocean to the steady-state mixture at the ocean base (i.e., from $X_{1,0} = 0.02$ to $X_{1,b} = 0.37$ for the ^{16}O - ^{79}Se system); this could happen, e.g., when $\nabla > \nabla_{\text{ad}}$ at the top of the ocean. In the current paper we remove the inconsistency by allowing the composition at the top of the ocean to be different from that provided by the burning layer (e.g., Fig. 2; see also figure 3 from Paper II), and use the stabilizing effect of the burning layer on convection as justification. If we instead fix $\{X_{1,0}\}$, we find that once the convection zone reaches the top of the ocean there is a flux at the outer boundary

$$F_{r,X_i}(y_0) = \dot{m} \Delta X_{i,0c} \quad (\text{B13})$$

[Eqs. (10) and (29)], with $X_{i,0} \neq X_{i,c}$ because the system is not yet in steady state. In the O-Se system, this means that a large quantity of oxygen is being ejected from the ocean into the envelope, a fact that we are ignoring because of our assumption of a fixed envelope composition. We conclude that the only way to make our models consistent with a $\nabla > \nabla_{\text{ad}}$ ocean is to consider the envelope, by either allowing ocean material to mix into the envelope [through Eq. (B13)], or by including hydrogen and helium burning in the envelope to prevent mixing (as in Fig. 2).

HEAT AND COMPOSITION SOURCES

Here we derive expressions for the sources ϵ_{X_i} and ϵ , as used in the continuity equation Eq. (10) and entropy balance equation Eq. (11), respectively.

There are sources of composition change ϵ_{X_i} at three locations in our model:

1) At the ocean-crust boundary, composition changes abruptly due to chemical separation and rapid sedimentation of the solid at the phase transition. Formally, we write

$$\epsilon_{X_i} = -(\dot{m} - \dot{y}_b) \Delta X_{i,bc} \delta(y - y_b), \quad (\text{C1})$$

where δ is the Dirac delta function; but in practice we simply adjust $X_{i,c}$ manually without reference to Eq. (10).

2) At the hydrogen and helium burning layer, composition changes quickly due to the strong temperature dependence of the thermonuclear reactions, from $\{X_{i,e}\}$ in the envelope to $\{X_{i,0}\}$ at the top of the ocean. We assume that the burning layer is infinitely thin, such that formally we have

$$\epsilon_{X_i} = \dot{m} (X_{i,0} - X_{i,e}) \delta(y - y_0). \quad (\text{C2})$$

Note that $X_{i,0}$ is not necessarily the value given by the burning layer ashes ($\{X_{\text{O}}, X_{\text{Se}}\} = \{0.02, 0.98\}$ for the O-Se ocean model of this paper); we allow $X_{i,0}$ to vary based on the composition profile required by efficient convection in the ocean (see Section 3).

3) In the crust, composition changes gradually due to electron captures and pycnonuclear fusion. For simplicity we set $\langle A \rangle_c = 56$ as the composition at the top of the crust, regardless of the value of $X_{i,c}$, and follow the procedure of BC09 to obtain $\langle Z \rangle$ and $\langle A \rangle$ at greater depths. With this approximation, $X_{i,c}$ only determines the physics of the liquid-solid phase transition [e.g., in Eq. (36)] and has no effect on the crust properties (thermal conductivity, etc.).

During accretion, there are heat sources ϵ at three locations in our model (see Fig. 5):

1) At the hydrogen and helium burning layer, particles are driven to a critical depth (temperature) for thermonuclear reactions by accretion; for $\{X_H, X_{He}\} = \{0.7, 0.3\}$ these reactions release $Q = 5$ MeV nucleon $^{-1}$ (e.g., Brown & Bildsten 1998). Following BC09, we assume that the heat is released uniformly in the logarithm of column depth, over a region from $y = y_{\text{low}}$ to y_{high} , such that

$$\epsilon = \begin{cases} \frac{Q\dot{m}/m_p}{y \ln(y_{\text{high}}/y_{\text{low}})}, & y_{\text{low}} < y < y_{\text{high}}; \\ 0, & \text{otherwise.} \end{cases} \quad (\text{C3})$$

Here we choose $y_{\text{low}} = 0.2y_0$ and $y_{\text{high}} = y_0$.

2) In the outer crust, electron captures release $Q = 0.2$ MeV nucleon $^{-1}$ (e.g., Haensel & Zdunik 2008); we use $y_{\text{low}} = 5 \times 10^{12}$ g cm $^{-2}$ and $y_{\text{high}} = 5 \times 10^{15}$ g cm $^{-2}$.

2) In the inner crust, pycnonuclear fusion reactions release $Q = 1.2$ MeV nucleon $^{-1}$; we use $y_{\text{low}} = 5 \times 10^{15}$ g cm $^{-2}$, and $y_{\text{high}} = 3 \times 10^{18}$ g cm $^{-2}$.

THERMODYNAMIC QUANTITIES

Here we derive or define expressions for several thermodynamic quantities in multicomponent plasmas that are used in this paper.

The total differential for the Gibbs free energy is given by

$$dG = -SdT + VdP + \sum_{i=1}^n \mu_i dN_i + \mu_e dN_e, \quad (\text{D1})$$

where G includes the energy of the ions and the electrons, V is the total volume, n is the total number of ion species in the plasma, μ_i is the chemical potential of ion species i , N_i is the number of ions of species i , μ_e is the electron chemical potential, and N_e is the number of electrons. Note that although $N_e = \sum_{i=1}^n Z_i N_i$ for the fully-ionized multicomponent plasma, such that N_e is not an independent thermodynamic variable, here we treat it as such in order to express the various relations derived in this section in terms of both ion and electron quantities. The ion and electron terms are combined in the rest of the paper [Eqs. (8) and (16)] to simplify the appearance of the equations. Using $X_i = A_i N_i / \langle A \rangle N$, $Y_e = \sum_{i=1}^n Y_i X_i$, and the Euler integral

$$G = \sum_{i=1}^n \mu_i N_i + \mu_e N_e, \quad (\text{D2})$$

where G is the Gibbs free energy, we have

$$dg = -sdT + \frac{1}{\rho} dP + \sum_{i=1}^n \frac{\mu_i}{A_i m_p} dX_i + \frac{\mu_e}{m_p} dY_e. \quad (\text{D3})$$

Here q is the “specific” version of the quantity Q ; i.e., $q = Q/M$, where $M = \langle A \rangle m_p N$ is the total mass of the system and $N = \sum_{i=1}^n N_i$ is the total number of ions. Using Eq. (D3) we can derive two useful Maxwell relations: Since

$$\left(\frac{\partial^2 g}{\partial X_i \partial T} \right)_{P, X_{j \neq i}, Y_e} = \left(\frac{\partial^2 g}{\partial T \partial X_i} \right)_{P, X_{j \neq i}, Y_e}, \quad (\text{D4})$$

we have

$$-\left(\frac{\partial s}{\partial X_i} \right)_{T, P, X_{j \neq i}, Y_e} = \frac{1}{A_i m_p} \left(\frac{\partial \mu_i}{\partial T} \right)_{P, X_i, Y_e}; \quad (\text{D5})$$

similarly,

$$-\left(\frac{\partial s}{\partial Y_e} \right)_{T, P, X_i} = \frac{1}{m_p} \left(\frac{\partial \mu_e}{\partial T} \right)_{P, X_i, Y_e}. \quad (\text{D6})$$

We define

$$b_{P,i} \equiv -X_i \left(\frac{\partial s}{\partial X_i} \right)_{T, P, X_{j \neq i}, Y_e} = \frac{X_i}{A_i m_p} \left(\frac{\partial \mu_i}{\partial T} \right)_{P, X_i, Y_e} \quad (\text{D7})$$

and

$$b_{P,e} \equiv -Y_e \left(\frac{\partial s}{\partial Y_e} \right)_{T,P,X_i} = \frac{Y_e}{m_p} \left(\frac{\partial \mu_e}{\partial T} \right)_{P,X_i,Y_e} ; \quad (\text{D8})$$

these terms are analogous to the ion and electron specific heat terms $c_{P,i} = T(\partial s_i / \partial T)_{T,P,X_i}$ and $c_{P,e} = T(\partial s_e / \partial T)_{T,P,Y_e}$ for the composition. For degenerate electrons

$$b_{P,e} = -\frac{\pi^2 k_B T}{3E_F} \frac{Y_e k_B}{m_p} = -\frac{2}{3} c_{P,e} , \quad (\text{D9})$$

where $E_F = m_e c^2 (\sqrt{1 + x_F^2} - 1)$ is the Fermi energy with $x_F = 10.0 \rho_9^{1/3} Y_e^{1/3}$; for the models we consider here the electrons are degenerate and Eq. (D9) holds throughout the ocean, since $k_B T / E_F \lesssim 0.2$ (for $\rho \gtrsim 10^6 \text{ g cm}^{-3}$ and $T \simeq 3 \times 10^8 \text{ K}$). An accurate expression for $b_{P,i}$ in the ocean can be obtained from $\mu_i = (\partial F_l / \partial N_i)_{T,V,N_{j \neq i}}$ and the free energy of a multicomponent liquid

$$F_l = k_B T \sum_{i=1}^n N_i \left[f_l^{\text{OCP}}(\Gamma_i) + \ln \left(\frac{N_i Z_i}{N_e} \right) \right] , \quad (\text{D10})$$

where f_l^{OCP} (including the ideal gas part) is defined in equations 1 and 2 of Medin & Cumming (2010); we use this accurate expression in our numerical calculations. However, an approximation for $b_{P,i}$ can be obtained by considering only the ideal gas term, the dominant temperature-dependent term in μ_i :

$$b_{P,i} \simeq \frac{X_i}{A_i m_p} k_B \ln \left[\frac{N_i}{V} \left(\frac{h^2}{2\pi A_i m_p k_B T} \right)^{3/2} \right] \sim 30 \frac{X_i k_B}{A_i m_p} \sim 10 c_{P,i} . \quad (\text{D11})$$

TRACKING THE OCEAN-CRUST BOUNDARY

Here we derive expressions for the motion of the ocean-crust boundary, as well as the changes in entropy and composition at the ocean crust boundary.

Using Eq. (6) and

$$\langle Z_b^{5/3} \rangle = \sum_{i=1}^n x_{i,b} Z_i^{5/3} = \langle A \rangle \sum_{i=1}^n X_{i,b} \frac{Z_i^{5/3}}{A_i} , \quad (\text{E1})$$

we have that the ocean-crust boundary moves at a rate

$$\dot{y}_b = \dot{y}_{b,T} + \dot{y}_{b,X} , \quad (\text{E2})$$

where

$$\dot{y}_{b,T} = \frac{\partial y_b}{\partial T_b} \frac{\partial T_b}{\partial t} = \frac{4y_b}{T_b} \frac{\partial T_b}{\partial t} \quad (\text{E3})$$

and

$$\dot{y}_{b,X} = \sum_{i=1}^n \frac{\partial y_b}{\partial X_{i,b}} \frac{\partial X_{i,b}}{\partial t} = \sum_{i=1}^{n-1} y'_{b,i} \frac{\partial X_{i,b}}{\partial t} \quad (\text{E4})$$

with

$$\frac{\partial y_b}{\partial X_{i,b}} = \frac{4y_b \langle A \rangle}{\langle Z_b^{5/3} \rangle} \frac{\langle Z_b^{5/3} \rangle - Z_i^{5/3}}{A_i} \quad (\text{E5})$$

and

$$y'_{b,i} = \frac{\partial y_b}{\partial X_{i,b}} - \frac{\partial y_b}{\partial X_{n,b}} . \quad (\text{E6})$$

For an ^{16}O - ^{79}Se mixture, $y'_{b,1} \simeq 10y_b$. At the ocean-crust boundary, the energy balance equation Eq. (11) in the frame moving with the boundary is

$$T_b \frac{\partial s_b}{\partial t} + T_b (\dot{m} - \dot{y}_b) \left. \frac{\partial s}{\partial y} \right|_{y=y_b^{\text{down}}} = \left. \frac{\partial F_r}{\partial y} \right|_{y=y_b} + \epsilon , \quad (\text{E7})$$

where y_b^{down} indicates that the derivative is evaluated on the “downstream” side of the boundary: y_b^+ during heating ($\dot{y}_b > 0$), and y_b^- during cooling ($\dot{y}_b < 0$). Note that $(\partial s / \partial y)_{y=y_b^+} = 0$ and that $\epsilon = 0$ during cooling.

For a two component mixture, near the base of the ocean $\nabla X_1 = \chi T (\nabla_{\text{ad}} - \nabla) / \chi_1 \ll 1$ (cf. Paper I), such that $\partial X_1 / \partial t$ is almost constant there. Therefore, using Eq. (35),

$$\frac{\partial X_{1,b}}{\partial t} \simeq \frac{\dot{m} \Delta X_{1,0c} - \dot{y}_b \Delta X_{1,bc}}{y_b}; \quad (\text{E8})$$

with Eqs. (E2)–(E4) we have

$$\frac{\partial X_{1,b}}{\partial t} \simeq \frac{1}{1 + y'_{b,1} \Delta X_{1,bc} / y_b} \left(\frac{\dot{m} \Delta X_{1,0c}}{y_b} - \frac{4 \Delta X_{1,bc}}{T_b} \frac{\partial T_b}{\partial t} \right). \quad (\text{E9})$$

During cooling we have from Eqs. (35) and (E9) that

$$4 \frac{\partial \ln T_b}{\partial t} \simeq \left(1 + \frac{y'_{b,1} \Delta X_{1,bc}}{y_b} \right) \frac{\partial \ln y_b}{\partial t}; \quad (\text{E10})$$

for $\Delta X_{1,bc} \ll 1$, $4(\partial \ln T_b / \partial t) \simeq \partial \ln y_b / \partial t$; while for $\Delta X_{1,bc} \sim 1$, $\partial \ln T_b / \partial t \sim 3(\partial \ln y_b / \partial t)$.

EFFECTS OF ROTATION AND MAGNETIC FIELD ON CONVECTION

The effects of rotation and magnetic fields on convection have been examined in many places (e.g., Stevenson 1979, 2003; Jones 2000; Christensen & Aubert 2006; see also Showman, Kaspi, & Flierl 2011). Here we use simple arguments to show that in the neutron star ocean, the efficient convection assumption Eq. (9) is very good even in the presence of rapid rotation ($\sim 10^2 \text{ s}^{-1}$) and moderate magnetic fields ($\sim 10^{10} \text{ G}$).

We consider a two-component ocean mixture with a plane-parallel geometry and governed by Newtonian physics. We impose a gravitational field $-g\hat{\mathbf{r}}$, rotation $\boldsymbol{\Omega}$, and magnetic field \mathbf{B}_0 , all uniform. We assume that during convective mixing, displaced fluid elements do not exchange heat or material with their surroundings until they have traveled a distance of order the mixing length l_m ; but by rapidly contracting or expanding they maintain pressure balance with their surroundings (cf. Appendix A). We therefore have

$$\left(\frac{dP_{\text{tot}}}{dr} \right)_{s,X,Y_e} = \frac{dP_{\text{tot}}}{dr}, \quad (\text{F1})$$

where $P_{\text{tot}} = P + P_{\text{mag}}$ and

$$P_{\text{mag}} = \frac{B^2}{8\pi}. \quad (\text{F2})$$

Note that the equations of Appendices D–B are unaffected by the inclusion of this magnetic “pressure” term because $P_{\text{mag}} \ll P$. In the rotating frame, the equation of motion for a fluid element displaced from its equilibrium position \mathbf{r}_0 is

$$\rho \frac{\partial \mathbf{v}}{\partial t} = f_{\text{grav}} + f_{\text{rot}} + f_{\text{mag}} \quad (\text{F3})$$

where

$$\mathbf{v} = \frac{\partial \delta \mathbf{r}}{\partial t}, \quad (\text{F4})$$

$$f_{\text{grav}} \simeq -g \left[\left(\frac{d\rho}{dr} \right)_{s,X,Y_e} - \frac{d\rho}{dr} \right] \delta r_r \hat{\mathbf{r}} \simeq \rho g \mathcal{A} \delta r \hat{\mathbf{r}} \quad (\text{F5})$$

is the buoyancy force (per unit volume) felt by the element,

$$f_{\text{rot}} = -2\rho \boldsymbol{\Omega} \times \mathbf{v} \quad (\text{F6})$$

is the Coriolis force, and

$$f_{\text{mag}} = \frac{1}{4\pi} (\nabla \times \mathbf{B}) \times \mathbf{B} + \nabla P_{\text{mag}} = \frac{1}{4\pi} (\mathbf{B} \cdot \nabla) \mathbf{B} \simeq \frac{1}{4\pi} (\mathbf{B}_0 \cdot \nabla) \delta \mathbf{B} \quad (\text{F7})$$

is the magnetic “tension” force. Here

$$\delta \mathbf{r} = \mathbf{r} - \mathbf{r}_0 \quad (\text{F8})$$

is the displacement of the element from its equilibrium position and

$$\delta \mathbf{B} = \mathbf{B} - \mathbf{B}_0 \quad (\text{F9})$$

is the perturbation to the magnetic field caused by this displacement. The magnetic tension term f_{mag} acts as a restoring force (cf. Kulsrud 2005): for a typical wavelength l_m and a perpendicular field displacement of $\delta \mathbf{r}$ we have that

$$\delta \mathbf{B} \sim \frac{B_0}{l_m} \delta \mathbf{r} \quad (\text{F10})$$

such that

$$f_{\text{mag}} \sim \rho \omega_B^2 \delta \mathbf{r}, \quad (\text{F11})$$

where

$$\omega_B^2 = \frac{B_0^2}{4\pi \rho l_m^2} = \left(\frac{v_A}{l_m} \right)^2 \quad (\text{F12})$$

and

$$v_A = \frac{B_0}{\sqrt{4\pi \rho}} \quad (\text{F13})$$

is the Alfvén velocity.

We assume that the rotation and magnetic fields are oriented in no particular direction relative to each other or the gravitational field: $\mathbf{\Omega} = \Omega_x \hat{\mathbf{x}} + \Omega_r \hat{\mathbf{r}}$ and $\mathbf{B}_0 = B_{0,x} \hat{\mathbf{x}} + B_{0,y} \hat{\mathbf{y}} + B_{0,r} \hat{\mathbf{r}}$, where $\Omega_x \sim \Omega_r$ and $B_{0,x} \sim B_{0,y} \sim B_{0,r}$. We then have the equations of motion

$$\frac{\partial^2 \delta r}{\partial t^2} \sim (g\mathcal{A} - \omega_B^2) \delta r + 2\Omega \frac{\partial \delta x}{\partial t} \quad (\text{F14})$$

and

$$\frac{\partial^2 \delta x}{\partial t^2} \sim -2\Omega \frac{\partial \delta r}{\partial t} - \omega_B^2 \delta x \quad (\text{F15})$$

(with the assumptions made above, δy is independent of δr and δx , and so we do not consider it further). If we assume that both δr and δx depend on t as $\exp(\sigma t)$, where σ is a constant, Eqs. (F14) and (F15) give

$$\sigma^4 + (2\omega_B^2 + 4\Omega^2 - g\mathcal{A})\sigma^2 \sim \omega_B^2(g\mathcal{A} - \omega_B^2). \quad (\text{F16})$$

Equations (B3) and (B5) for the composition and convective heat fluxes still apply when $B_0 \neq 0$ and $\Omega \neq 0$, except that v_{conv} there is now the convective velocity only in the radial direction. Equation (B2) no longer applies, however, since the force per unit mass on the displaced element is not given by just the buoyancy term Eq. (B1). Instead we use

$$v_{\text{conv},r} = \left. \frac{\partial \delta r}{\partial t} \right|_{\delta r = l_m/2} = \frac{1}{2} \sigma l_m. \quad (\text{F17})$$

The convective velocity must be large enough to carry the required composition flux Eq. (29); σ , the oscillation frequency for the convective instability, will grow until this happens. Comparing Eqs. (B3) and (29), we have that

$$\sigma l_m^2 \simeq \frac{4(\dot{m} - \dot{y}_b)}{\rho} \frac{\Delta X_{bc} H_P}{X \nabla_X}, \quad (\text{F18})$$

or assuming $l_m \sim H_P$ and $\dot{m} - \dot{y}_b \sim 10^5 \text{ g cm}^{-2} \text{ s}^{-1}$ (cf. Appendix B),

$$v_{\text{conv},r} \sim 10^{-2} \text{ cm s}^{-1} \quad \text{and} \quad \sigma \sim 10^{-5} \text{ s}^{-1}. \quad (\text{F19})$$

For transiently accreting neutron stars $\Omega \sim 10^2 \text{ s}^{-1}$ and $B_0 \lesssim 10^{10} \text{ G}$, such that $\Omega \gtrsim \omega_B \gg \sigma$. Therefore we have from Eq. (F16) that

$$g\mathcal{A} \simeq \omega_B^2, \quad (\text{F20})$$

and that

$$\sigma^2 \sim \frac{\omega_B^2}{\omega_B^2 + 4\Omega^2} (g\mathcal{A} - \omega_B^2). \quad (\text{F21})$$

From Eq. (F21) we see that $\sigma < 0$, and therefore convection is inhibited, until the convective discriminant is at least as large as ω_B^2/g ; i.e., until the buoyancy force exceeds the magnetic tension force. A slight excess of $g\mathcal{A}$ over ω_B^2 gives the composition flux necessary to transport the chemical imbalance at the base of the ocean.

Since $\mathcal{A} = \chi_T (\nabla - \nabla_{\text{ad}}) / (\chi_\rho H_P) + \chi_X \nabla_X / (\chi_\rho H_P) \simeq \omega_B^2/g \sim 10^{-10} \text{ cm}^{-1}$ while $\chi_T (\nabla_{\text{ad}} - \nabla) / (\chi_\rho H_P) \sim 10^{-6} \text{ cm}^{-1} \gg \mathcal{A}$, we have

$$\chi_X \nabla_X \simeq \chi_T (\nabla_{\text{ad}} - \nabla); \quad (\text{F22})$$

i.e., the efficient convection assumption Eq. (9) is good even in the presence of rotation and magnetic fields.

Note that there is some ambiguity in the typical length scale for the problem. Putting Eq. (F21) back into Eqs. (F14) and (F15) gives

$$\delta x \sim \frac{2\Omega\sigma}{\omega_B^2} \delta r; \quad (\text{F23})$$

since $\sigma \ll \omega_B$, the typical perturbation in the horizontal direction is much smaller than in the vertical direction. This may require an average displacement smaller than $l_m/2$ to be used in Eq. (F17) (see, e.g., Stevenson 1979), which will increase the oscillation frequency σ required to generate the composition flux F_X . However, we still have $\sigma^2 \ll g\mathcal{A}$

such that $g\mathcal{A}$ will not change much (unless ω_B also changes) and our conclusion remains the same. Note also that if the star is non-magnetic such that $\omega_B = 0$, Eq. (F16) instead gives

$$\sigma^2 \sim g\mathcal{A} - 4\Omega^2 \quad (\text{F24})$$

and we have

$$\mathcal{A} \simeq 4\Omega^2/g \sim 10^{-10} \text{ cm}^{-1}; \quad (\text{F25})$$

we again find that efficient convection is a good assumption.

REFERENCES

- Altamirano, D., Keek, L., Cumming, A. et al. 2012, MNRAS, 426, 927
- Bildsten, L. & Brown, E. F. 1997, ApJ, 477, 897
- Bildsten, L. & Cutler, C. 1995, ApJ, 449, 800
- Brown, E. F. 2004, ApJ, 614, L57
- Brown, E. F. & Bildsten, L. 1998, ApJ, 496, 915
- Brown, E. F., Bildsten, L., & Chang, P. 2002, ApJ, 574, 920
- Brown, E. F. & Cumming, A. 2009, ApJ, 698, 1020
- Cackett, E. M., Brown, E. F., Cumming, A., Degenaar, N., Fridriksson, J. K., Homan, J., Miller, J. M., & Wijnands, R. 2013, ApJ, 774, 131
- Cackett, E. M., Wijnands, R., Linares, M., Miller, J. M., Homan, J., & Lewin, W. H. G. 2006, MNRAS, 372, 479
- Cackett, E. M., Wijnands, R., Miller, J. M., Brown, E. F., & Degenaar, N. 2008, ApJ, 687, L87
- Christensen, U. R. & Aubert, J. 2006, Geophys. J. Int., 166, 97
- Cox, J. P. 1980, Theory of Stellar Pulsation (Princeton: Princeton)
- Cumming, A. & Bildsten, L. 2001, ApJ, 559, L127
- Cumming, A., Macbeth, J., in 't Zand, J. J. M., & Page, D. 2006, ApJ, 646, 429
- Degenaar, N., Medin, Z., Cumming, A., et al. 2014, ApJ, submitted
- Degenaar, N. & Wijnands, R. 2011, MNRAS, 412, 68
- Degenaar, N., Wolff, M. T., Ray, P. S., et al. 2011, MNRAS, 412, 1409
- Degenaar, N., Wijnands, R., Brown, E. F., et al. 2013a, ApJ, 775, 48
- Degenaar, N., Wijnands, R., & Miller, J. M. 2013b, ApJ, 767, L31
- Fridriksson, J. K., Homan, J., Wijnands, R., et al. 2011, ApJ, 736, 162
- Gupta, S., Brown, E. F., Schatz, H., Möller, P., & Kratz, K.-L. 2007, ApJ, 662, 1188
- Haensel, P. & Zdunik, J. L. 1990, A&A, 227, 431
- Haensel, P. & Zdunik, J. L. 2008, A&A, 480, 459
- Horowitz, C. J., Berry, D. K., & Brown, E. F. 2007, Phys. Rev. E, 75, 066101
- Hughto, J., Horowitz, C. J., Schneider, A. S., Medin, Z., Cumming, A., & Berry, D. K. 2012, Phys. Rev. E, 86, 066413
- Hughto, J., Schneider, A. S., Horowitz, C. J., & Berry, D. K. 2011, Phys. Rev. E, 84, 016401
- in 't Zand, J. J. M., Cumming, A., van der Sluys, M. V., Verbunt, F., & Pols, O. R. 2005, A&A, 441, 675
- in 't Zand, J. J. M., Kuulkers, E., Verbunt, F., Heise, J., & Cornelisse, R. 2003, A&A, 411, L487
- Keek, L., in 't Zand, J. J. M., Kuulkers, E., Cumming, A., Brown, E. F., & Suzuki, M. 2008, A&A, 479, 177
- Kippenhahn, R. & Weigert, A. 1994, Stellar Structure and Evolution (Berlin: Springer)
- Kulsrud, R. M. 2005, Plasma Physics for Astrophysics (Princeton: Princeton)
- Kuulkers, E. 2002, A&A, 383, L5
- Kuulkers, E., in 't Zand, J. J. M., Homan, J., van Straaten, S., Altamirano, D., & van der Klis, M. 2004, in AIP Conf. Proc. 714, X-Ray Timing 2003: Rossi and Beyond, ed. P. Kaaret, F. K. Lamb, & J. H. Swank (Melville, NY: AIP), 257
- Heney, L. & L'Ecuyer, J. L. 1969, ApJ, 156, 549
- Homan, J., van der Klis, M., Wijnands, R., et al. 2007, ApJ, 656, 420
- Jones, C. A. 2000, Philos. Trans. R. Soc. A, 358, 873
- Medin, Z. & Cumming, A. 2010, Phys. Rev. E, 81, 036107
- Medin, Z. & Cumming, A. 2011, ApJ, 730, 97
- Medin, Z. & Cumming, A. 2014, ApJ, 783, L3
- Page, D. & Reddy, S. 2013, Phys. Rev. Lett., 111, 241102
- Piro, A. L. & Bildsten, L. 2005, ApJ, 619, 1054
- Potekhin, A. Y., Baiko, D. A., Haensel, P., & Yakovlev, D. G. 1999, A&A, 346, 345
- Potekhin, A. Y. & Chabrier, G. 2000, Phys. Rev. E, 62, 8554
- Schatz, H., Bildsten, L., Cumming, A., & Wiescher, M. 1999, ApJ, 524, 1014
- Schatz, H., Aprahamian, A., Barnard, V., et al. 2001, Phys. Rev. Lett., 86, 3471
- Schatz, H., Bildsten, L., Cumming, A., & Ouellette, M. 2003, Nucl. Phys. A, 718, 247
- Showman, A. P., Kaspi, Y., & Flierl, G. R. 2011, Icar., 211, 1258
- Stevens, J., Brown, E. F., Cumming, A., Cyburt, R., & Schatz, H. 2014, ApJ, 791, 106
- Stevenson, D. J. 1979, Geophys. Astrophys. Fluid Dynam., 12, 139
- Stevenson, D. J. 2003, Earth Planet. Sci. Lett., 208, 1
- Strohmayer, T. E. & Brown, E. F. 2002, ApJ, 566, 1045
- Wijnands, R., Guainazzi, M., van der Klis, M., & Méndez, M. 2002, ApJ, 573, L45
- Wijnands, R., Homan, J., Miller, J. M., & Lewin, W. H. G. 2004, ApJ, 606, L61
- Wijnands, R., Miller, J. M., Groot, P. J., Markwardt, C., Lewin, W. H. G., & van der Klis, M. 2001, ApJ, 560, L159
- Wijnands, R., Nowak, M., Miller, J. M., Homan, J., Wachter, S., & Lewin, W. H. G. 2003, ApJ, 594, 952
- Woodruff, D. P. 1973, The Solid-Liquid Interface (London: Cambridge)
- Woosley, S. E., Heger, A., Cumming, A., et al. 2004, ApJS, 151, 75